JGR Solid Earth

RESEARCH ARTICLE
10.1029/2022JB025666

Key Points:

- 2D-discrete element method simulations performed on numerical fault gouges composed of a very dense assembly of polygonal-shaped particles
- A small change in grain-scale gouge properties impacts Riedel shear band formation, their orientation angle and the type of Riedel structure formed
- High interparticle friction and high bulk shear modulus increase the breakdown energy and the occurrence of dynamic slip instabilities

Supporting Information:

Supporting Information may be found in the online version of this article.

Correspondence to:

N. Casas,
nath27casas@gmail.com

Citation:

Casas, N., Mollon, G., & Daouadji, A. (2023). Influence of grain-scale properties on localization patterns and slip weakening within dense granular fault gouges. *Journal of Geophysical Research: Solid Earth*, *128*, e2022JB025666. https://doi.org/10.1029/2022JB025666

Received 21 SEP 2022
Accepted 9 MAR 2023

Author Contributions:

Conceptualization: N. Casas
Data curation: N. Casas
Formal analysis: N. Casas
Investigation: N. Casas
Methodology: N. Casas, G. Mollon
Software: N. Casas, G. Mollon
Supervision: G. Mollon, A. Daouadji
Validation: G. Mollon, A. Daouadji
Visualization: N. Casas
Writing – original draft: N. Casas
Writing – review & editing: N. Casas, G. Mollon, A. Daouadji

Influence of Grain-Scale Properties on Localization Patterns and Slip Weakening Within Dense Granular Fault Gouges

N. Casas[1,2,3], G. Mollon[1], and A. Daouadji[2]

[1]University Lyon, INSA-Lyon, CNRS UMR5259, LaMCoS, Villeurbanne, France, [2]University Lyon, INSA-Lyon, GEOMAS, Villeurbanne, France, [3]Earth Sciences Department, Sapienza University of Rome, Rome, Italy

Abstract Fault zones are usually composed of a granular gouge, coming from the wear material of previous slips, which contributes to friction stability. When considering a mature enough fault zone that has already been sheared, different types of infill materials can be observed, from mineral cementation to matrix particles that can fill the remaining pore spaces between clasts and change the rheological and frictional behaviors of the gouge. We aim to understand and reproduce the influence of grain-scale characteristics on slip mechanisms and gouge rheology (Riedel bands) by employing the discrete element method. A 2D-direct shear model is considered with a dense assembly of small polygonal cells of matrix particles. A variation of gouge characteristics such as interparticle friction, gouge shear modulus or the number of particles within the gouge thickness leads to different Riedel shear band formation and orientation that has been identified as an indicator of a change in slip stability. Interpreting results with slip weakening theory, our simulated gouge materials with high interparticle friction or a high bulk shear modulus, increase the possible occurrence of dynamic slip instabilities (small nucleation length and high breakdown energy). They may give rise to faster earthquake ruptures.

Plain Language Summary The center of a seismic fault zone is usually composed of a material with granular particles highly contributing to the way the fault moves. This zone may be composed of various infill materials from mineral cementation to smaller particles that can fill the remaining pore spaces between larger particles and change the properties of the fault zone. We aim to understand and reproduce the influence of grain-scale characteristics on slip mechanisms by employing numerical simulations. A variation of granular particle characteristics leads to different deformation patterns that can be identified as an indicator of a change in slip stability. The obtained results suggest that some granular materials with high interparticle friction or a high bulk shear modulus, increase the possible occurrence of dynamic slip instabilities which may lead to faster earthquake ruptures. This work investigates in more depth the link between the characteristics of the granular material, the deformations of the fault core, and the possible occurrence of an earthquake.

1. Introduction

Within the fault core, the fault gouge is known to deeply contribute to friction stability (Marone & Scholz, 1988; Reches & Lockner, 2010) and to play an important role in the sudden energy release during seismic sliding (Sammis et al., 1987). For local fault scale studies, one of the key points remains to be able to relate geological and physical properties of the gouge to the slip behavior and types of dynamic slip instabilities (Collettini et al., 2019; Leeman et al., 2015;). One way to determine the laboratory rock failure stability is to compare K, the loading stiffness of the fault, with its weakening rate K_c. Based on stick-slip theory (Byerlee & Brace, 1968; Marone, 1998; Scholz & Engelder, 1976)], slip instabilities may occur if the loading stiffness of the fault K (i.e., stiffness of the loading system) is lower than K_c ($K_c > K$). The friction obtained during gouge sliding can then be modeled either with classical slip-dependent laws (Campillo & Ionescu, 1997; Palmer & Rice, 1973; Tullis, 2015) or rate-and-state friction laws (Dieterich, 1979; Lockner & Beeler, 2002; Marone & Saffer, 2015) to infer on dynamic slip occurrence and behaviors (Dieterich, 1972; Im et al., 2019; Ohnaka, 2013; Scholz et al., 1972; Scuderi et al., 2020; Spagnuolo et al., 2016).

The weakening rate is also related to the breakdown energy released during the slip. The total energy budget ΔW (J.m^{-2}) associated with this rupture propagation, also based on classical slip weakening models (Abercrombie & Rice, 2005; Aubry et al., 2018; Kanamori & Heaton, 2000; Rice & Cocco, 2002), is the total deformation energy dissipated in the fault process and the sum of a breakdown energy E_B (on-fault energy), a radiated energy

E_R (off-fault energy propagating by the mean of elastic waves) and a frictional energy E_H (dissipated within the slip zone by frictional heating). The post-peak rupture energy E_B, or breakdown energy, is the energy needed to weaken the fault. While E_B was often assimilated to the fracture energy G_c (Abercrombie & Rice, 2005), it is now useful to differentiate that the breakdown work appears to be the sum of the fracture energy (the very first peak of weakening) and the overshoot energy or other second weakening process (Casas et al., 2022; C. Y. Ke et al., 2022; Paglialunga et al., 2021). In this paper, we restrict our focus to the kinematics of granular localization and its effect on friction evolution with slip. We neither take into account the second-order change in friction due to a small change in velocity (rate-and-state friction), nor the first-order change in friction due to temperature increase and heat production with high slip-rate (thermal weakening mechanisms), (Di Toro et al., 2006; Niemeijer et al., 2011; Rice, 2006).

Previous analysis of fault zone rheology has shown that the onset of instabilities requires some shear localization, that is, fault fabric development (Palmer & Rice, 1973), although the reverse proposition is not necessarily true (Moore et al., 1989). These shear deformations are complex structures, that can be observed at specific Riedel angles (Tchalenko, 1970). They have been the subject of considerable interest for many years (Byerlee, 1978; Hadizadeh et al., 2015; Haines et al., 2013; Y. Katz & Weinberger, 2005; Riedel, 1929; Scuderi et al., 2020), and reflect a heterogeneous stress field developing in response to deformation (Kaminskaite et al., 2019; Marone & Scholz, 1989; Morgan & Boettcher, 1999). The presence of these Riedel bands has been identified as potentially responsible for mechanical weakening (Beeler et al., 1996; Gu & Wong, 1994) and they can be both associated with slow-slip events or fast earthquakes (Bürgmann & Dresen, 2008; Ferri et al., 2011; Gu & Wong, 1994; Hadizadeh et al., 2015; Scuderi et al., 2017). The angle between Riedel bands and the direction of shearing, depending on the physical properties of the fault gouge, is also an indicator of a change in slip stability (Byerlee et al., 1978). However, the link between the angle orientation of Riedel bands and slip patterns is not yet fully understood.

In this paper, we study the slip mechanism and the frictional response of sheared gouge materials in quasi-static conditions. We also consider an over-consolidated material for which both the density and strength of the material are supposed to have increased with time under compaction with high normal stress (Morrow & Byerlee, 1989). This can originate from cementation due to rock dissolution or partial melting (Di Toro et al., 2009; Fondriest et al., 2020; Rodrigues et al., 2021; Walderhaug, 1994), from local comminution (i.e., wear particle formation) or from the introduction of other sediments within the fault gouge (Lee & Kim, 2005; Woodcock & Mort, 2008). In Casas et al. (2022), we simulated a cemented granular fault gouge (dry contact) with 2-D Discrete Element Modeling (DEM), establishing a link between the initial amount of porosity and cementation within the gouge and the type of rheological behavior observed. In order to have a better understanding of the link between grain-scale properties and gouge-scale deformations through Riedel bands evolution, another 2D-DEM model is proposed herein, composed of thin matrix particles (i.e., very thin cohesionless particles) with no variation in grain size distribution. This granular medium represents a highly dense packing of particles revealing Riedel band formation with direct shear experiments. This work is seen as the first step toward simulations considering a mixture of angular grains surrounded by matrix cells representing a matrix of fines. The objective is to better understand the influence of some grain-scale properties on the entire deformation of the gouge. The first section presents the numerical model and granular samples used for the study. Then the second part of this paper is devoted to the study of the timing of Riedel band formation and evolution as a function of gouge characteristics. All the lithologic variations presented are then summarized into only three main parameters: the interparticle friction (micro-scale), the effective shear modulus of the gouge layer (macro-scale), and the ratio of gouge thickness to grain size (i.e., number of particles within the gouge thickness). In the last section, the roles of these three parameters are discussed by comparing Riedel angle orientation and effective friction peak. Then, the obtained results are interpreted according to a very simplified model such as the linear slip weakening model, to establish a connection with the occurrence of dynamic slip instabilities.

2. Methodology for Sheared Fault Gouge Modeling

Even though certain continuous methods are used to model geological fault structures (Lynch & Richards, 2001), they commonly face difficulties in reproducing experimental observations due to the continuity assumption they need to adopt. As an alternative to the classical finite element method (FEM) and finite difference method (FDM), the discrete element method (DEM) describes the flow of granular materials where each particle has its own behavior and interactions with its neighbors (Cundall & Strack, 1979; Potyondy & Cundall, 2004). The DEM has been successfully used in fault mechanics to understand some frictional and contact properties inside the fault core (Aharonov & Sparks, 2004; Cho et al., 2008; Da Cruz et al., 2005; Dorostkar et al., 2017a; Dorostkar et al., 2017b; Ferdowsi et al., 2014; Ferdowsi & Rubin, 2020; Gao et al., 2018; Guo & Morgan, 2004; Mollon et al., 2021; Morgan, 1999; Morgan & Boettcher, 1999; Zhao et al., 2012; Zhao, 2013). DEM enables us to observe the nucleation and propagation of discrete structures during shearing. In this study, the code MELODY2D is used for the simulation of a 2D-DEM fault gouge (Mollon, 2016; Mollon, 2018). This C++ code allows us to simulate a broad variety of granular media in two dimensions. In this numerical framework, each particle has its own motion and trajectory, driven by Newton's laws of motion. The contour of each grain is discretized by a piecewise linear frontier with nodes and segments, and a two-pass node-to-segment contact algorithm is employed to avoid interpenetrations (Casas et al., 2022; Mollon, 2018). The motion is controlled by user-defined and physics-based contact interactions, Figure 1a. In the present case, a Coulomb friction contact law is also adopted, meaning that every contact between particles depends on the interparticle friction μ_{num}, normal and tangential contact stiffnesses k_n and k_t and numerical damping γ. Typical grain interpenetrations under the applied normal stress and with the chosen contact stiffness remain below 1% of the typical grain size.

We also underline the importance of using non-circular particles for rigid bodies, since this choice has a strong influence on the effective friction measured within the gouge (Anthony & Marone, 2005; Mair et al., 2002; Mollon et al., 2020; Nouguier-lehon et al., 2003). A granular sample with only matrix particles is created as a dense assembly of small polygonal cells, Figure 1b. To generate this kind of granular medium, a code called Cvoro (C++) using a Voronoï tessellation algorithm (Mollon & Zhao, 2012) allows the creation of a dense packing of polygonal particles. A simplification has been made on this granular material, which will allow us to observe the influence of the size distribution of the particles and porosity knowingly of grain-scale influence. This work is seen as the first step toward future simulations considering mixtures of angular grains surrounded by matrix cells representing a matrix of fines.

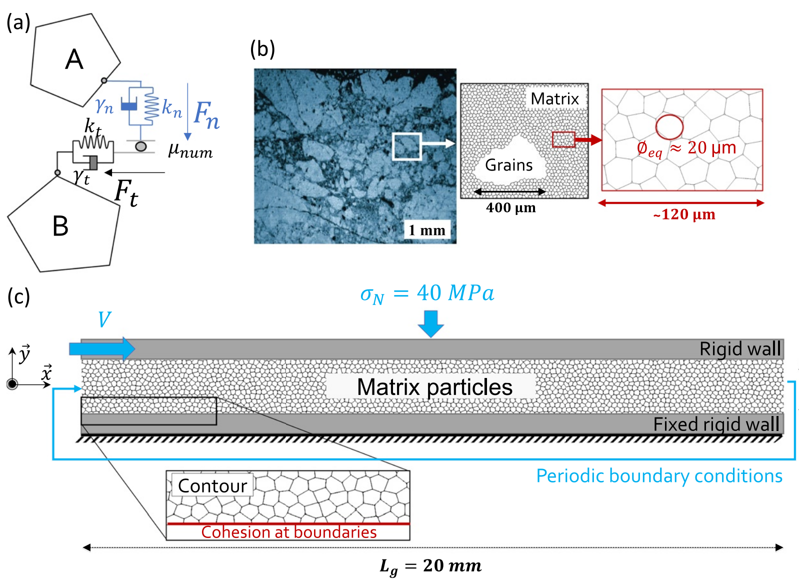

Figure 1. (a) Sketch of a digital elevation model (DEM) contact between two particles A and B, constituted by interparticle friction μ_{num}, stiffness $k_n = k_t$, and damping $\gamma = \gamma_n = \gamma_t = 0.2$ which are numerical parameters; (b) Matrix material shape and size: left, image from Riedmüller et al. (2001); center, modelization with angular particles and matrix particles; right, zoom in on matrix particles with grains of equivalent diameter $\Phi_{\mathrm{eq}} = 20\ \mu$m; (c) DEM model of a direct shear experiment with granular fault gouge composed of 115,825 matrix particles (for the reference sample). V is the applied shearing velocity of 1 m/s for quasi-static conditions, σ_N is the normal stress of 40 MPa, th_i is the initial gouge thickness of 2 mm (only for the reference sample) and the length of the gouge $L_g = 20$ mm. The first simulation step consists in compacting the sample with a normal stress of 40 MPa to create a stabilized packing of granular material. As the generated sample is already very compact, this compaction stage is only influenced by the numerical stiffness and interparticle friction inserted between particles in contact. At the end of the compaction, the sample is almost identical, but with a little interpenetration between particles (less than 1% of the size of the particle) which provides mechanical equilibrium.

10.1029/2022JB025666

To be able to realize parametric studies, a "Matrix-Sample" (M-S) is defined as a reference sample (summary of characteristics in Text S1 and Table S1 in Supporting Information S1). The initial porosity within the gouge is negligible here ($\ll 1\,\%$), resulting in an extremely dense compacted sample, to simulate the behavior of an over-consolidated material (Lambe & Whitman, 1991). A constant particle size is considered ($\varnothing_{eq} \approx 20\,\mu$m), with slightly irregular polygons, Figure 1b. An initial gouge thickness th_i equal to 2 mm was chosen to be consistent with the literature of laboratory experiments (Giorgetti et al., 2019; Scuderi et al., 2014; Scuderi et al., 2017, among others), or other DEM fault gouge shear experiment (Dorostkar et al., 2017a). The length of the gouge L_g is then set to 20 mm in order to have a representative surface element and be able to observe sufficient shear deformations (Casas et al., 2021). For the numerical campaign, other gouge samples are also created (a) by changing the regularity (i.e., angularity): of polygonal particles created from regular hexagons (sample a2) to highly angular particles (sample b2), Text S8 and Figure S10 in Supporting Information S1; (b) by changing the size of particles created as $\varnothing_{\mathrm{eq}} \approx 30, 40$, and $50\,\mu$m; (c) by changing the thickness of the gouge th_i from 1 mm (sample c) to 4 mm (sample d). Details on the numerical parameters used for all samples modeled can be found in Table S3 and S4 in Supporting Information S1.

The granular matrix is then deformed with direct shear experiments (Figure 1c). The lower rock wall is fixed in displacement while a normal stress of 40 MPa and a shearing velocity of $1\ \mathrm{m/s}$ are imposed on the upper rock wall. The shearing velocity has been chosen to maintain the inertial number lower than 10^{-3} in order to avoid any inertial effect with the gouge shearing and to remain in a quasi-static granular flow (Da Cruz et al., 2005), Text S6 in Supporting Information S1. In this model, the use of a high velocity should not be confused with the one used in laboratory experiments. It allows the simulations to run in a reasonable time duration and has no consequence on the way the fault is deforming (Text S7, Figures S8 and S9 in Supporting Information S1). In other words, time is an irrelevant physical quantity in this quasi-static simulation, and is merely an evolution parameter. This is acceptable since phenomena such as heat production or contact aging are disregarded. Periodic boundary conditions are present on both right- and left-hand sides of the sample to maintain the continuity of the movement at large slips, but the upper rock wall can freely move in the y-direction to allow dilatancy to take place.

A dry contact model is considered with rigid bodies for both particles and rock walls (rock density equal to 2,600 $\mathrm{k\ g/m^3}$). Gravity is ignored in the model, assuming that the fault can be oriented in a wide range of directions, and that gravity forces are negligible compared to those related to normal and deviatoric stresses applied on the gouge. For the sample (M-S), μ_{num} is equal to 0.3 to test the property of matrix particles as low-friction material, k_n and k_t are constant and equal to $10^{15}\ \mathrm{Pa/m}$ (Casas et al., 2022). Finally, to avoid wall-slip effects which occur with smooth boundaries, an arbitrarily high cohesion of 500 MPa is introduced at the interface between matrix and rock walls. It enables the creation of a certain roughness by cementing particles of the top and bottom layers to their respective boundaries. Finally, independent numerical biaxial simulations were run (Text S2 and Figure S1 in Supporting Information S1) to recover Mohr-Coulomb data (internal friction angle φ, cohesion C, and elastic modulus E), and compare numerical samples to real rock ones (Table S2 and Figure S2 in Supporting Information S1). For (M-S), a cohesion $C = 6.4$ MPa is observed with an internal friction angle φ equal to 43.3° (i.e., corresponding to a friction peak $\mu_p = 0.94$). The resulting elastic modulus E equals 19 GPa.

In this model, some physical phenomena are not taken into account. Grain fragmentation is disregarded because grain breakage is not a common feature of DEM and is not implemented in our code. More information on dedicated techniques can be found in Zhao (2013) and Wang et al. (2021). Also, the temperature increase is not be considered with shearing (although it can technically be done in other contexts, see, e.g., Mollon et al., 2021), meaning that no heat-related effect can appear. Finally, no particle deformation or chemical interactions are implemented in the present simulations.

3. Results

3.1. Results for the Reference Sample

This subsection aims to present the results obtained for the reference granular sample (M-S), as it will be used for comparison in the rest of the paper. Typical effective friction $\mu^* = \tau/\sigma_N$, total tangential force $\tau \cdot L_g$ resisting fault sliding, divided by the applied normal force $\sigma_N \cdot L_g$, and dilation $\varepsilon_y = \Delta\mathrm{th}/_{\mathrm{th_i}}$, the thickness variation Δth in the vertical direction, divided by the initial granular sample thickness, are presented in Figure 2. Shear deformation profiles are observed at different times of the simulation thanks to the solid fraction which enables us to easily observe slip and shear concentration with changes in porosity (Figure 3).

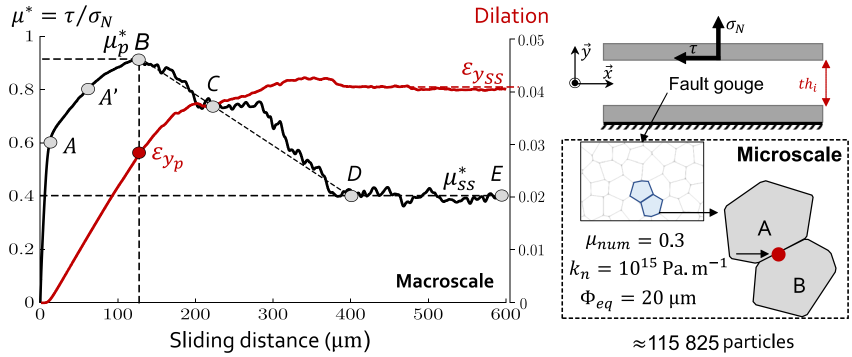

Figure 2. Effective friction μ^* (black curve) and dilation ε_y (red curve) as a function of the slip distance (μ m) of the upper rock wall for the reference sample (M–S). A is the end of the elastic stage. The stage from zero to B describes the pre-peak phase, followed by the slip-weakening stage (B to D) and then by the steady-state stage (D to E). ε_{y_p} represents the critical dilation, that is, the dilation at friction peak. It is also important to note the difference between the effective friction peak μ_p^* (maximum effective friction) and the steady-state effective friction μ_{ss}^*, which is the average value of the effective friction once the plateau is reached for a constant applied shearing velocity. The effective friction is not to be confused with the Mohr-Coulomb friction coefficient μ_f, or the interparticle friction μ_{num}.

In the friction curve, four main stages are highlighted with increasing slip (Figures 2 and 3), consistent with the main stages of Riedel shear formation (Marone, 1998). First, a pre-peak stage is observed, composed of an elastic phase (0-A) allowing to define of the shear modulus of the gouge. As dilation has not started yet, no significant volumetric deformation is observed within the gouge. Second, the sample is deforming in a non-reversible way until the friction peak (A-B), for which the maximum shear strength of the gouge is reached (B). During this stage, the sample dilates (red curve), with a critical dilation ε_{y_p} still lower than the averaged steady-state dilation $\varepsilon_{y_{SS}}$. Riedel shear bands (i.e., R-bands), appear as the following with shearing: primary R-bands R_3, R_4, and R_5, are first activated just before friction peak, and followed by secondary R-bands R_1 and R_2 at effective friction peak, with slightly lower Riedel angle orientation α_i. Third, during the slip weakening stage, or post-peak stage (B to D), the friction gradually decreases until it reaches a friction plateau and maximum dilation at D. In this stage, primary R-bands give way to the two mains secondary R-bands R_1 and R_2, which localize all the gouge deformation (Figure 3). A boundary shear Y_1 also starts growing at the top of the gouge layer propagating from one R-band to another. In fact, it can be identified that the softening part between C and D corresponds to this propagation: going progressively from a fully coupled to a fully sliding Y-band, which causes this softening (Movie S1). Finally, once the steady-state is reached (stage from D to E), the gouge reaches a stationary state of evolution. The friction then fluctuates very weakly around a mean value which is similar in most of the simulations and ranges between 0.4 and 0.5. From this moment, the dilation of the granular sample is maximum and stabilized. In this regime, the main R-bands do not evolve anymore and seem de-activated, a secondary Y_2-band is partly observed at the bottom rock wall, and the Y_1-band is fully formed at the top rock wall (D) and accommodates all the relative velocity (Movie S2).

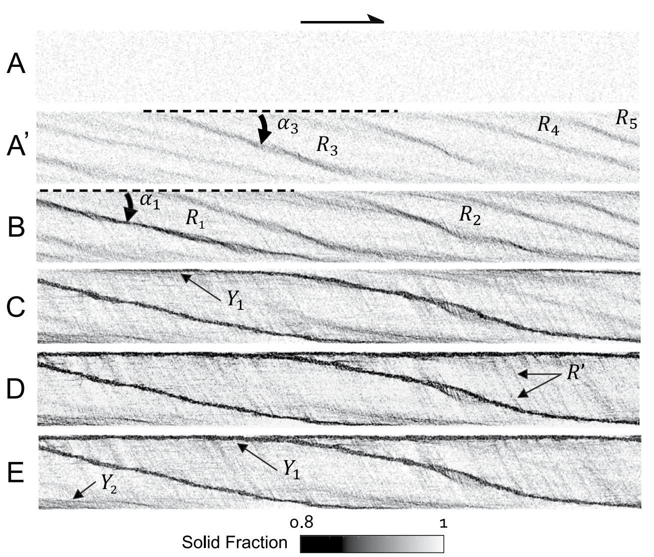

Figure 3. Solid fraction snapshots for reference sample (M–S). The solid fraction is used here to observe the rheology and deformations within the granular gouge. It is the ratio between the total surface of particles on the total surface of the gouge (particles and voids). In the present case, it is plotted as a field, that is, each pixel corresponds to the value of the solid fraction in its close neighborhood. The solid fraction is plotted between 0.8 and 1. Letters correspond to different steps in the effective friction curve in Figure 2. R_1 and R_2 are secondary R-bands, R_3, R_4, and R_5 are primary R-bands, orientated at angle α_i from the direction of shearing. R'-bands are incipient conjugate Riedels, orientated at angle α'_i from the direction of shearing. Y is the slip localization at the boundary: Y_1 is the main localization occupying all the slip surface and Y_2 is a partially developed boundary at the opposite surface (Movie S1).

Conjugate Riedel bands (i.e., R'-bands) are also observed in the simulations, oriented at about $\alpha' \approx 60°$ from the top wall (Figure 3d). They present a higher angle orientation than for simple tensile T-bands (oriented in the direction of the major principal stress at 45°), but lower than that described for R'-bands observed in the literature, which approaches 75° (Davis et al., 2000; Y. Katz et al., 2004). It is assumed that these bands are T-bands rotating toward R'-bands. Moreover, the theory of Riedel bands is based on

10.1029/2022JB025666

the Mohr-Coulomb model, which is an idealized model that does not consider the post-peak decrease of the shear resistance. We consider that the bands observed between 50 and 60° are R'-bands according to their connections with the observed R-bands.

3.2. Link Between Particles Characteristics, Friction, and Rheology

To characterize this matrix material, a series of parametric studies were performed, varying geometrical (shape, size) or physical (interparticle stiffness and friction) properties of the matrix to represent different rock lithologies. These studies were done not only to observe the influence of each parameter on the mechanical behavior but also to observe how each characteristic is linked to the rheological behavior through R-band formation and evolution. All these lithologic variations are summarized into only three parameters: the interparticle friction μ_{num} (microscale), the effective shear modulus $G = \tau/_{\varepsilon}$ (at the macroscale, the ratio between the shear stress τ and shear strain ε in the elastic regime), and the ratio of gouge thickness to grain size n_p (i.e., number of particles within the gouge thickness).

3.2.1. Influence of Interparticle Friction on Riedel Shear Band Orientation

A change in interparticle friction coefficient μ_{num} from 0.1 to 0.6 yields a significant increase in effective friction peak values, and a small increase in the steady-state effective friction as shown in Figure 4a. When increasing μ_{num}, the slip weakening behavior thus evolves from a small $\Delta\mu = \mu_p^* - \mu_{ss}^*$ with large critical distance of slip D_c (low μ_{num}), to a high $\Delta\mu$ with smaller D_c (high μ_{num}), (Figure 5 (ii)). An increment in the interparticle friction also drastically increases the orientation angle of the main R-bands from the beginning of the simulation and until steady-state, ($\alpha_i \approx 6°$ for $\mu_{\mathrm{num}} = 0.1$ and $\alpha_i \approx 16°$ for $\mu_{\mathrm{num}} = 0.6$), Figures 4b and 5. Increasing μ_{num} also increases the number of R-bands formed during shearing, resulting in a reduced average distance between two successive bands. These results are consistent with Lefevre et al. (2020) and Jiao et al. (2021) who reproduced sandboxes with different widths and found a link between the internal friction angle and the distance between R-bands.

Riedel structures, that is, the combination between R-bands and R'-bands, are also observed at steady-state for a low μ_{num}. However, only R-bands are observed with increasing μ_{num} at steady-state (Figure 5). We carried out a similar study by slightly changing the shape of particles, giving more or less regularity and therefore more or less angular polygons (Figures 4 and 5). The results are consistent with Mair et al. (2002) and Nouguier-lehon et al. (2003) and show that the increase of angularity increases the effective friction peak. Moreover, the angularity of particles seems to favor the development of R-bands (Figure 5b (b2)). In the same way as interparticle friction, a higher angularity in the shape of particles results in a larger number of R-bands at the friction peak. These R-bands are also less marked and of lower thickness than (M-S). However, the change of angle orientation at steady-state is very small (<12% of the relative difference in α_i), meaning that the angularity of particles is too limited to have a major influence on R-band angle orientation.

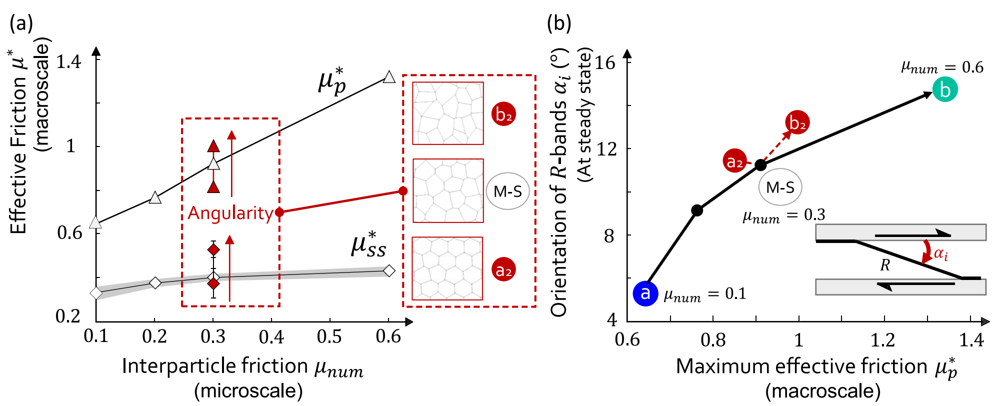

Figure 4. (a) Effective friction at peak μ_p^* and steady state μ_{ss}^*, as functions of inter-particle friction. And the effect of an increase in particles angularity (in red, from samples a2 to b2), Text S8 and Figure S10 in Supporting Information S1; (b) orientation angle of Riedel bands α_i (°) as a function of the effective friction peak for a variation in interparticle friction (black curve), from (a) to (b), or of the angularity of particles (red curve). Letters a, b, and b2 refer to Figure 5 for gouge kinematics.

10.1029/2022JB025666

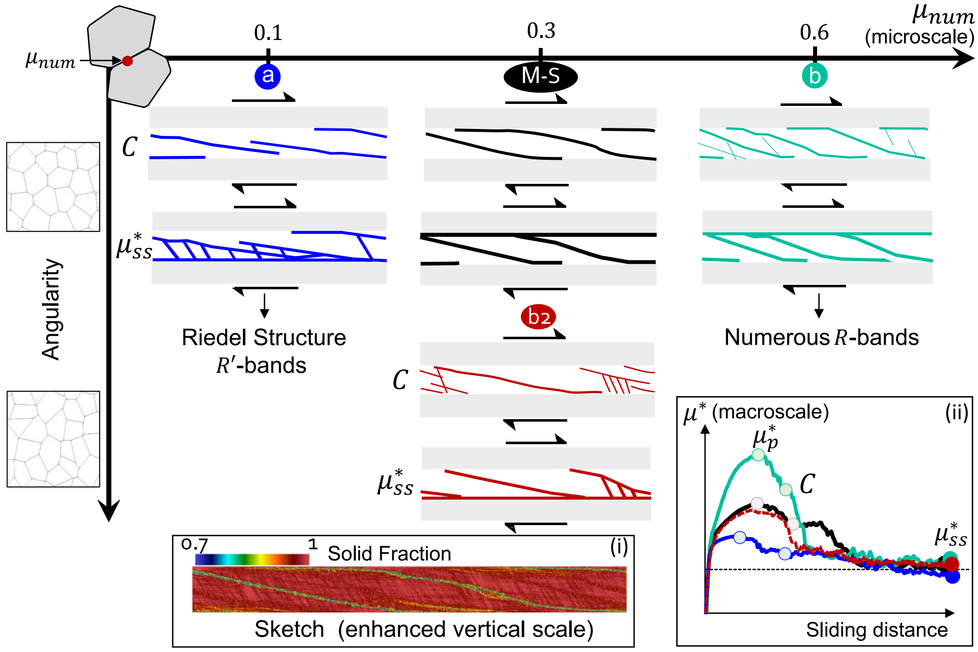

Figure 5. Riedel patterns as a function of the interparticle friction (horizontal axis) and the angularity (vertical axis), during the weakening part (C), or at steady-state (μ^*_{ss}). (i) Illustrative solid fraction map used for sketches—Reference sample (M–S) at point C. (ii) Effective friction as a function of the sliding distance for four different samples. More information on the change in the angularity of particles can be found in Text S8 and Figure S10 in Supporting Information S1.

3.2.2. Influence of Shear Modulus on Riedel Structure

We observe in Figure 6a that an increase in the interparticle stiffness (purple) and an increase in the particle size (orange) both lead independently to an increase in the shear modulus G_S, Figure S4 in Supporting Information S1. Concerning the grain size effect, it is clearly a modeling artifact: a sample with large grains is simply stiffer because the number of elastic accommodation sites (interparticle contacts) is reduced while their compliance is constant, thereby artificially stiffening the granular assembly. In the remainder of the paper, we will only deal with the increase in shear modulus coming from an increase in the contact stiffness between the particles.

The shape of friction curves is compared in Figure 6b, for two samples with different shear modulus: (M-S) with $G_S = 5.52$ GPa and (g) with $G_S = 41.9$ GPa. In DEM model, the numerical stiffness is only supposed to act on the overlapping of particles that controls the elastic part of the effective friction curve: an increase in interparticle

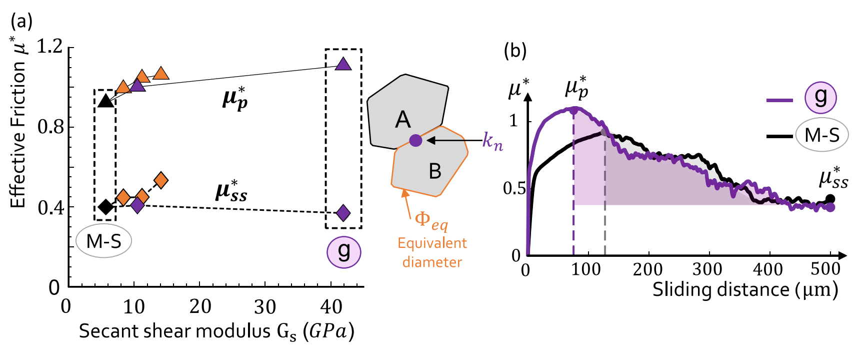

Figure 6. (a) Effective friction as a function of secant shear modulus G_s (GPa) for friction peak μ^*_p and steady state friction μ^*_{ss}. The increase in shear modulus corresponds to an increase in interparticle stiffness (purple points, 10^{15}, 2 10^{15} and 10^{16}) and to an increase in the size of particles (orange points, 20, 30, 40, and 50 μm with the same interparticle stiffness of 10^{15} Pa/m). Details on shear modulus calculation and values are in (Figure S3, Text S3, and Table S3 in Supporting Information S1). (b) Effective friction profile of sample (M–S) and sample (g).

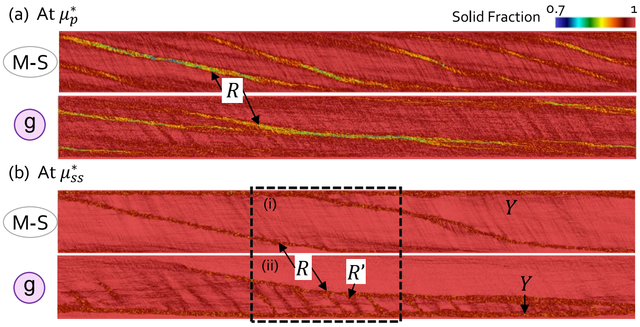

Figure 7. The solid fraction is between 0.7 and 1 for samples (M–S) and (g). (a) at effective friction peak μ_p^* and (b) at steady-state μ_{SS}^*. For an increase in shear modulus, the Y-localization occurred on the lower part of the gouge, as the entire upper part moves as one unit, unlike the (M–S) material which localizes at the top, due to the left $\boldsymbol{R}$-band which only allows part of the gouge to move along the x-axis.

stiffness increases the global stiffness, and thus the shear modulus. But, more surprisingly, an increase in shear modulus also increases both the effective friction peak (Figure 6a), and the total energy released during the weakening phase (Figure 6b).

Figure 7 gives a better understanding of how shear modulus affects $\boldsymbol{R}$-band formation by showing simulation snapshots of $\boldsymbol{R}$-bands for samples (M-S) and (g) (letter in Figure 6). The orientation angle of the main $\boldsymbol{R}$-band band α_i is reduced from 12° (M-S) to 7° (g). From friction peak to steady state, an increase in G_s completely changes the kinematics inside the gouge (Figures 7a and 7b). In sample (g), only one single $\boldsymbol{R}$-band is observed, running the length of the gouge and having two slopes with different orientations (at boundaries). A Riedel structure is formed with many $\boldsymbol{R'}$-bands (Figure 7b), as opposed to the reference sample (M-S), where no clear Riedel structure is observed. Hence, an increase in shear modulus not only leads to a decrease in the angle orientation of the main $\boldsymbol{R}$-bands but also the formation of a complex Riedel structure. Figure 7 only shows the sample with the highest shear modulus, but the intermediate samples show a progressive evolution of the rheology from samples (M-S) to (g). More results can be found in appendix Text S9 and Figure S11 in Supporting Information S1.

$\boldsymbol{R}$'-bands are rarely observed in the field because of their short lifespan (compared to $\boldsymbol{R}$-bands) and limited thickness. They rotate at a higher speed than the $\boldsymbol{R}$-bands and usually disappear as they grow (Logan et al., 1992; Morgan & Boettcher, 1999; Morrow & Byerlee, 1989). That is why in several studies (R. Katz et al., 2006; Schmocker et al., 2003), the $\boldsymbol{R}$-bands are the only bands observed. In this study, $\boldsymbol{R'}$-bands are very pronounced in the sample with the highest shear modulus. These $\boldsymbol{R'}$-bands are present during the whole simulation and seem to be responsible for the difficulty of the material in the sample (g) to deform by shearing, inhibiting multiple $\boldsymbol{R}$-band formations. The distribution of force chains in the two types of gouges, Figure 8, allows us to better understand the formation of $\boldsymbol{R'}$-bands. In both samples the total transmitted force is similar, but the transmission of forces goes through different paths. In areas without $\boldsymbol{R}$-bands, the material is very compacted and the force transmission is diffuse (i.e., continuum-like). Within $\boldsymbol{R}$-bands, where the localization of deformation takes place, the material is granular with high porosity (varying with shearing between 10% and 20%), so force chains are very localized, forming a rather discrete network. On the other hand, the junctions between the different bands are places of stress concentrations, reflecting kinematic incompatibilities. It can also be noted that the observed thickness of $\boldsymbol{R'}$-bands is thus linked to the magnitude and width of the force chains network: $\boldsymbol{R'}$-bands will have a higher thickness (more visible) for stiffer or stronger materials with a higher magnitude of force chains. An overview of force chains within the material can therefore help to characterize the different types of deformations related to the two types of Riedel bands.

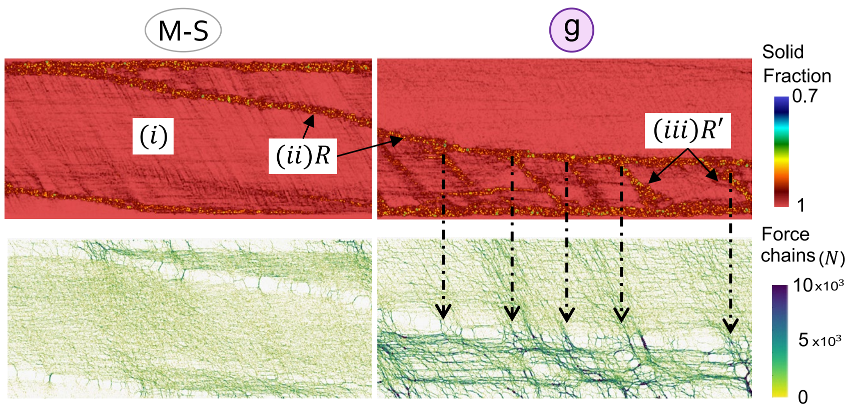

Figure 8. Zoom in on Figure 7b. The solid fraction is shown between 0.7 and 1 and a snapshot of force-chains networks is plotted from 0 to 10^4 N. Force chains are defined according to the typical level of stress present in the system (here the applied normal stress) and thickness and color are evaluated between the minimum and maximum contact force (0 to 10^4 N). A cut-off is made at 10^4 N to have the same visualization for all samples (higher force chains are observed for higher stiffness).

3.2.3. Influence of the Number of Particles Within the Gouge Thickness

Figure 9 presents the angle orientation of the main R-bands, α_i, as a function of the number of particles n_p in the gouge thickness th_i, which is also the ratio between gouge thickness and the size of particles. Hence, a change in n_p is tested by changing two parameters: a modification in the initial gouge thickness with the same size of particles (green), and an increase in the size of particles, with the same initial thickness and with a corrected stiffness effect (blue, keeping the shear modulus constant by decreasing interparticle stiffness).

A modification of n_p alone has no important influence on the shear modulus, nor on the observed effective friction (Text S4 and Figure S5 in Supporting Information S1). However, a link is found between n_p and the type of Riedel structure formed. Reducing the number of particles in the thickness tends to favor the formation of a Riedel structure composed of many R'-bands and for which the orientation of R-bands is lower (Figures 9c and 9e). This confirms that α_i is not only a material property but also depends on other fault properties. Some very thin gouges were also modeled with extremely low n_p (th$_i$ = 200 μm, 10 particles), and it was found that a minimal n_p (around 10–15 particles) is necessary to observe any slip localization and deformation in our simulations. Below this number, bulk shearing of the whole gouge is observed. This low number of particles can be related to a very young fault where few wear particles would yet be formed (Scholz, 1987). On the other hand, a very large n_p favors a multiplication of R-bands with a higher orientation angle. This result was only partially discussed in the literature, in the sense that particle size evolution was found to be responsible for the R-band angle as well as the gouge thickness, but the link between these two parameters was less investigated. When increasing the initial gouge thickness, a change in orientation is observed close to the boundaries, which may come from effects due to the larger sample size. Besides, fault gouges with an identical number of particles within the gouge thickness, and no variation of shear modulus will show the same effective friction and deformations (Text S5 and Figure S6 in Supporting Information S1).

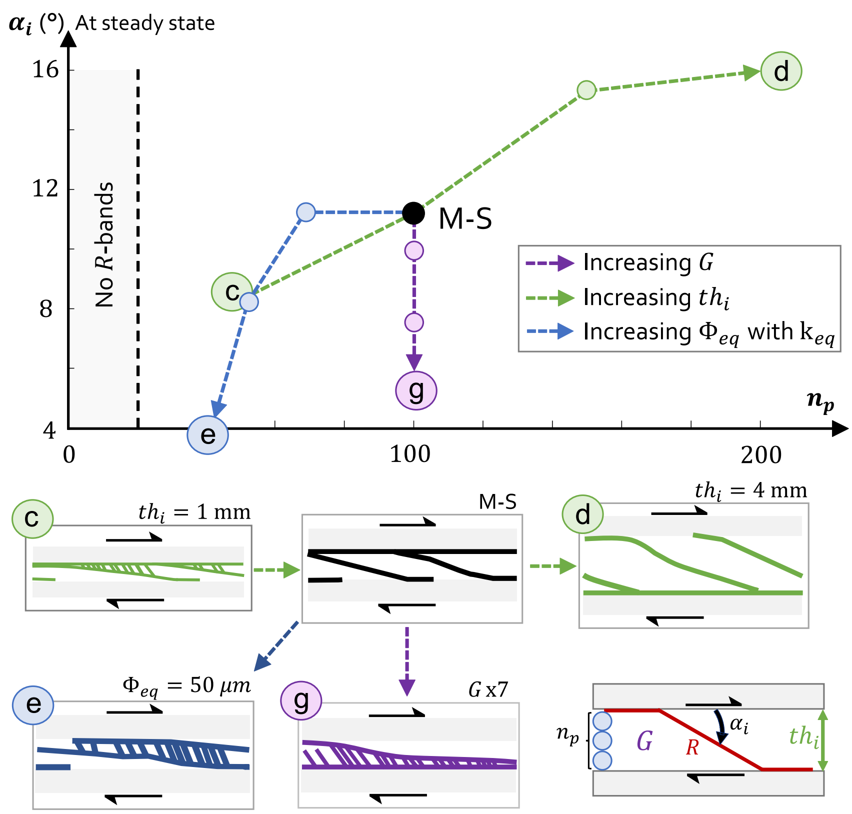

Figure 9. Schematic view of the angle orientation of the main R-bands α_i as a function of the ratio n_p, with distinction between three increasing parameters: (c) to (d) increase in the gouge thickness th_i, (M–S) to (e) increase in the size of particles Φ_{eq} with corrected contact stiffness k_{eq} to keep the same shear modulus for each gouge, (M–S) to (g) increase in the shear modulus G. The sense of the arrow represents an increase of all the parameters previously presented as detailed within the legend. Riedel structure patterns are represented below the figure and correspond to the extreme samples of the numerical campaign at steady-state. Details on Shear modulus values can be found in Table S3 in Supporting Information S1.

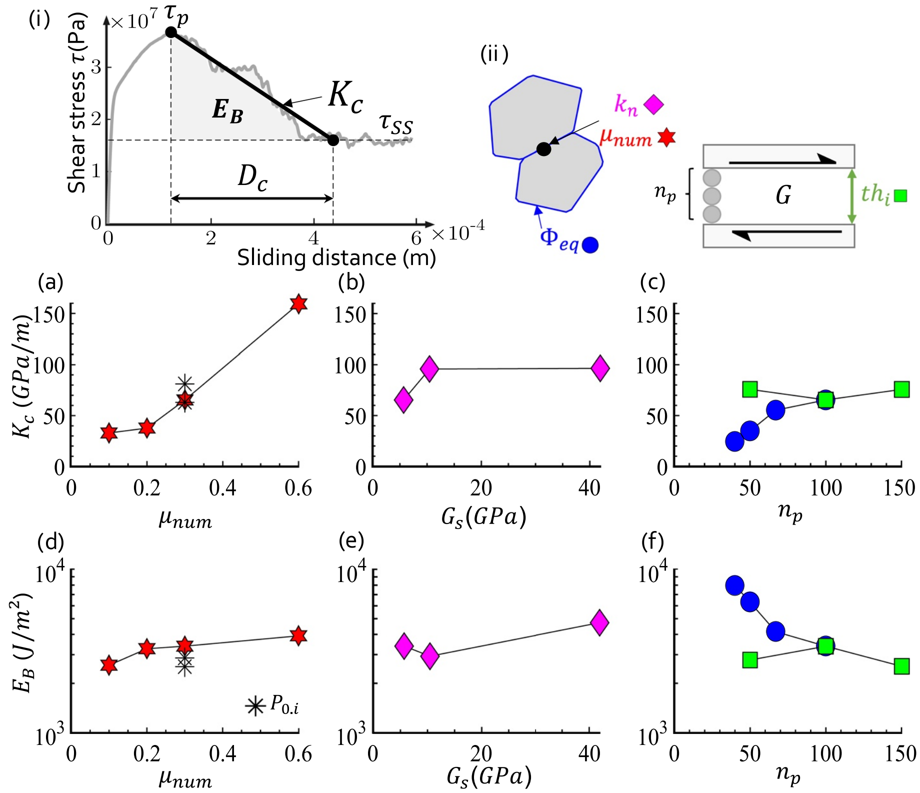

Figure 10. (i) Reference sample (M–S) results where the shear stress variation (Pa) is observed as a function of the slip distance (m). The slope K_c is calculated to have the same energy in J/m^2 for the triangle generated by the slope line than the E_B (colored in gray). With τ_p the maximum shear stress (Pa), τ_{ss} the dynamic (or steady-state) shear stress (Pa) and D_c the critical slip weakening distance (m). In this figure K_c fits well with the shape of the decreasing shear stress, but it is not as satisfactory for all the samples tested, Figure S7 in Supporting Information S1. (ii) Legend with color-coded shapes; Evolution of the critical weakening slope as a function of: (a) the interparticle friction, (b) the secant shear modulus G_s, and (c) the number of particles within the gouge stiffness. Evolution of the breakdown energy as a function of (d) the interparticle friction, (e) the secant shear modulus G_s, and (f) the number of particles within the gouge stiffness. Each graph represents the influence of a certain variable on the evolution of K_c out E_B, but we have only shown the data that changes with the indicated abscissa.

3.2.4. Slip Weakening and Breakdown Energy

In faults, the sliding is driven by the elasticity of the surrounding medium, and can therefore take place either in a stable or unstable manner depending on the fault's mechanical properties and boundary conditions. In the proposed models the sliding is imposed by artificial boundary conditions (imposed slip velocity) and we aim to reproduce local micromechanical behavior within the fault gouge. These models are designed to be inserted in larger-scale dynamic models (under the form of friction laws) to infer the stable or unstable character of the fault. To have a broader understanding of our gouge sample behavior, our results are first interpreted through the slip weakening theory.

The well-known critical slip distance D_c is the slip distance corresponding to a drastic decrease in frictional strength (Ohnaka, 2003; Ohnaka & Yamashita, 1989; Rabinowicz, 1951). We can thus define the slope of friction drop or weakening rate (in Pa/m) (Scholz, 2002), as follows

$$K_c = \frac{|\mu^*_{ss} - \mu^*_p|}{D_c}\sigma_N \tag{1}$$

Slip instabilities may occur if the loading stiffness of the fault K (i.e., stiffness of the loading system) is lower than K_c ($K_c > K$) (Scholz, 2002). The linear fitting of the weakening part of the effective friction curve may however induce errors because this weakening is sometimes governed by power laws (Abercrombie & Rice, 2005; Cocco et al., 2023). We, therefore, adopt a different approach to determine the weakening slope K_c, which is related to the breakdown energy released during the slip. In our model, E_B can be calculated as the area under the friction-slip curve (Palmer & Rice, 1973), corrected by subtracting the steady-state friction, and will lead to the calculation of the weakening slope (Figure 10i):

$$(\tau_p - \tau_{ss}) * \frac{D_c}{2} \equiv E_B = \int_0^{D_c^+} \left(\mu^*(U) - \mu^*_{SS}\right)\sigma_N \, d_U \tag{2}$$

Where $\left(\mu^*(U) - \mu^*_{SS}\right)\sigma_N$ is equal to $(\tau(U) - \tau_{SS})$, where D_c^+ is any sliding distance larger than D_c, and where the lower bound of the integral corresponds to the instant of the peak, from which D_c is considered. D_c is therefore inverted from the peak and steady-state frictions and from the breakdown energy required to slide from the former to the latter.

As observed in Section 3.2, an increase in interparticle friction μ_{num} increases exponentially K_c value (Figure 10a), whereas an increment in shear modulus G_s or number of particles n_p also increase the value of K_c but toward a plateau value (Figures 10b and 10c). Then, a small increase in breakdown energy E_B is observed by increasing μ_{num} and G_s (Figures 10d and 10e), whereas a higher increase in E_B is observed when decreasing n_p (Figure 10f).

4. Discussion on Gouge Rheology and Slip Weakening

4.1. Link Between Gouge Characteristics and Riedel Bands Patterns

A small change in gouge characteristics, (μ_{num}, n_p, G_s), impacts R-band formation through their orientation angle α_i and the type of Riedel structure formed. It is interesting to note that all the tested parameters influence α_i in a certain way, meaning that R-bands are not only linked to the external loading conditions but also depend on internal fault gouge properties, (Figure 11). As previously highlighted, three relevant quantities control the principal orientation angle of R-bands at steady-state: the interparticle friction μ_{num}, the number of particles within the gouge thickness n_p, and the effective shear modulus G_s. Figure 11 presents the angle orientation α_i of the main R-bands as a function of the effective friction peak, for all the studied samples compared to the standard sample (M-S) described in Section 3.1.

Figure 11 zone (i) gathers fault gouges with a high μ_{num} or a high n_p. These parameters increase the orientation angle α_i of R-bands and the number of R-bands appearing during the simulation (from effective friction peak to steady-state). This is a typical result of Mohr-Coulomb's theory (Gu & Wong, 1994; Y. Katz et al., 2004;

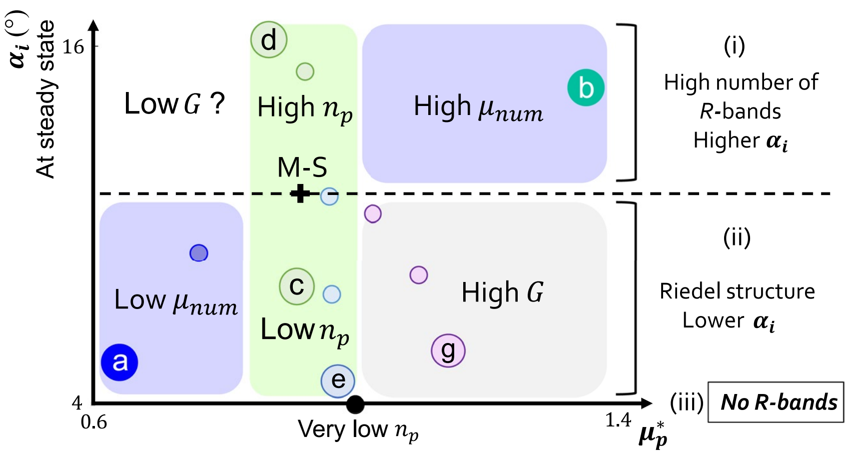

Figure 11. Schematic view of the orientation of R-bands α_i at steady-state as a function of the effective friction peak μ_p^*, with distinction between six major zones of interest: reduction or increase of interparticle friction μ_{num} , reduction or increase of n_p (without modification of the shear modulus) and reduction or decrease of the effective gouge shear modulus G. This graph only presents the R-bands patterns at steady-state because α_i variations with other instants of the simulation are not very significant (~ 1° − 2°). These variations were not studied in the present study but could be monitored at a different moment of the simulation (elastic phase, effective friction peak, weakening part…) in future research work.

10.1029/2022JB025666

Tchalenko, 1970) plotted the evolution of Riedel angles α_i as a function of effective friction and also found an increase in α_i with the increase of internal friction angle. The theory requires an angle equal to $\alpha_i = \varphi/2$ for direct shear (φ internal friction angle), but the value of φ can be questioned: should it be the one of the peak or the one of the plateau? The former seems inaccurate as numerical values of α_i are smaller than theoretical ones (which should be equal to 21.5° for the (M-S) sample, Table S2 in Supporting Information S1). The latter does not work either, because the plateau is at the same friction coefficient for all samples, whereas the α_i values can vary a lot. For a granular material, it appears that α_i is not only a material property (i.e., Mohr-Coulomb), but also a structural property changing with the shape, size, and stiffness of particles, the thickness of the fault, and the way particles interact and re-arrange with shearing.

By increasing only μ_{num} (i.e., due to mineral transformation, chemistry, surface, and grain shape roughness), both the maximum shear stress, and thus μ_p^* are increased without changing the shear modulus. The increase of K_c with high μ_{num} can be quite influential as it also implies a reduction of D_c (inversely proportional to K_c) and thus leads to a more sudden post-peak weakening. This could promote unstable slip, depending on the stiffness of the surrounding medium (i.e., stiffness of the damaged and intact rock). Materials with high interparticle friction coefficient (and low stiffness) are also known to present greater slip and a decrease in the recurrence time between two slip events (Dorostkar & Carmeliet, 2019).

At constant grain size, increasing the gouge thickness automatically increases n_p. Interpreted in terms of real fault, these n_p variations could correspond to different locations within the fault that could have lived different wear processes. For these materials μ_p^* slightly decreases and the orientation angle of R-bands increases. According to (Scholz et al., 1972), an accumulation of gouge layers tends to stabilize the system, and according to (Moore & Byerlee, 1992)'s theory, small Riedel angles also tend to stabilize the system. In our case, it seems that we have two competing effects: an increase in both the thickness of the gouge layer and in the orientation angle of the R-bands. These results could also be related to the stick-slip phenomenon obtained by (Lyu et al., 2019) when testing a variability of gouge thickness with different normal stresses. They observed that an increase in layer thickness, (i.e., an increase in the number n_p) implies a reduction of stress drop and friction and has a significant effect on stick-slip. On the top left of the graph, we notice an area without measurement points. Following the logic of the graph, we suppose that it corresponds to fault gouges with a very low shear modulus. This result remains to be verified with future simulation or experimental results.

Conversely, Figure 11 zone (ii) gathers fault gouges with a low μ_{num}, a low n_p, or a high G. For these materials, a similar rheological behavior is observed with a decrease in the orientation angle α_i of R-bands and the presence of a well-formed Riedel structure at steady-state (R-bands and R'-bands). The mechanical or physical changes applied to the fault gouge enhance the lifespan of R'-bands in their maximum size, explaining why more Riedel structures are observed.

Materials with low μ_{num} show a reduction in the maximum effective friction μ_p^*. These materials present lower R-bands angle α_i and a highly visible Riedel structure, and also increase D_c (which is inversely proportional to the low K_c observed), promoting slip stability. From the point of view of (Moore & Byerlee, 1992), they are prone to enhance stability within the gouge sample by reducing the stress drop. They could be related to weak gouges behavior (Bedford et al., 2022; Collettini et al., 2019) which are supposed to have very small effective friction. As opposed, materials with high G_s produce a higher resistance to slipping μ_p^*. The stiffness of the fault was found to depend on the ratio of the shear modulus to the size of the rupture nucleation zone (Leeman et al., 2016). A reduction in n_p is not necessarily linked to an increase in shear modulus, and the effective friction peak μ_p^* is almost not affected.

For very "young" fault gouge with a very thin granular layer (extremely low $n_p \ll 10 - 15$ grains), and for any combination in the other gouge characteristics, R-bands formation is prevented (Figure 11 (iii)). The maximum shear stress also increases whereas the dilation is slightly reduced for a reduction in fault gouge thickness, as previously found by (Biegel et al., 1989). This means that in order to observe shear localization in fault gouges, they must be mature enough to have a sufficiently thick gouge to allow R-band localization. In laboratory experiments, this mechanism may be slightly attenuated since we observe fragmentation of particles, which also allows shear localization (Bedford & Faulkner, 2021; Scuderi et al., 2017).

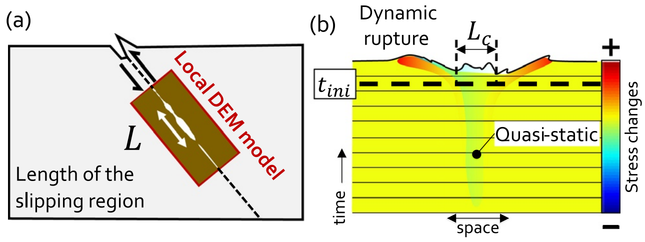

Figure 12. (a) A schematic figure showing the nucleation length L on a frictional fault plane. (b) Initiation of dynamic rupture from a smooth nucleation model, (figure redrawn from McLaskey (2019) and original from Ohnaka and Shen (1999)).

4.2. Occurrence of Dynamic Slip Instabilities

Fault mechanics often explores stick-slip instabilities, considering strain energy storage either at the grain scale (Dorostkar et al., 2018; Leeman et al., 2015) or in the loading system (Kasyap & Senetakis, 2021), and shearing experiments can thus be carried out in a stable or unstable way. In our model, the sliding is imposed by a shearing velocity, and the non-deformability of the rock does not allow a proper energy storage within the fault system. Even if kinetic energy is observed during the simulation due to particle interactions, the rigidity of the rock walls prevents direct comparison with papers showing stick-slip experiments. The purpose of this model is not to reproduce stick-slip, but to extract a frictional response in quasi-static conditions and observe the associated deformation within the microstructure. Our model is a zoom in a small patch within a large fault and provides information on the mechanical and rheological behavior of the fault. It cannot generate by itself a dynamic rupture and need to be combined with other dynamic models such as a 1D-spring slider (Bolotskaya & Hager, 2022) or spectral boundary integral element method (Romanet & Ozawa, 2022) to be able to properly see the different phases of the earthquake cycle. In the following, we propose a way to connect our rheological and mechanical data to nucleation properties.

Even though K_c can be extracted from each shearing result, the difficult question remains: what is the stiffness of the crust, and to what quantity K should the shear stiffness be compared? In laboratory experiments, K should be the stiffness of the loading apparatus, but for numerical experiments, we don't have such a value to consider. From crack theory, the global loading stiffness K is defined by the ratio of stress to displacement (Fialko, 2007; Griffith, 1924). The fault stiffness K is found to be proportional to the ratio $G/_L$, with G the shear modulus and L the length of the slipping fault section, meaning that the loading stiffness decreases as the slipping fault section increases, Figure 12a. If the slipping region is treated as an elliptical crack (Scholz, 2002), the critical nucleation length before dynamic slip instabilities L_c can be calculated as

$$L_c = \frac{E}{2(1-\nu^2)K_c} \tag{3}$$

E is the Young's modulus (or equivalent elastic modulus) of the surrounding rock, ν the Poisson ratio and K_c the critical weakening slope. The fault is unstable when the slipping fault section L exceeds the critical nucleation length L_c (Ohnaka & Shen, 1999). Figure 12b illustrates the dynamic behavior observed when L_c is reached, with a sudden transition to an unstable slip

From our numerical data, we can use Equation 3 to obtain the nucleation length L_c. The objective here is not to predict the "exact" value of L_c, but to observe trends and to put forward a dependence of L_c on certain gouge characteristics. The linear slip weakening approximation allows us, for each numerical sample, to link the value of L_c and E_B with the observed rheology of gouges. At a first glance, the nucleation length is observed to evolve linearly with the increase of the breakdown energy (Figure 13a). Around this trend, several outliers deserve to be mentioned. The area (i) gathers simulations performed with low inter-particle friction, they result in a higher L_c than the standard sample (M-S) and a rather low breakdown energy E_B. In this sample, there is much more mobility within the fault due to the large associated D_c. When n_p is reduced, in zone (ii), the observed breakdown energy E_B increases as well as the critical nucleation length L_c. The mechanical behavior is similar to the one of weak materials, but with a material that needs more fault displacement to stabilize (very large D_c in sample (e), Table S4 in Supporting Information S1), explaining the higher fracture energy observed. This very large D_c decreases the likelihood of dynamic instabilities to occur, but that they will present a larger stress drop should they happen. These two samples showed Riedel structure during the steady state of sliding. In zone (iii), fault gouge materials with high G_s or high μ_{num}, produce a higher resistance to sliding, giving a shorter nucleation length and medium breakdown energy value. A rather unstable behavior could be observed as a smaller slip is needed before dynamic slip instabilities happen. However, the link is still not clear between Riedel structures and dynamic slip stabilities because this zone (iii) presents different localization patterns at steady-state with a Riedel structure for a high G and only R-bands for high μ_{num}, despite the similar value for breakdown energy and nucleation length.

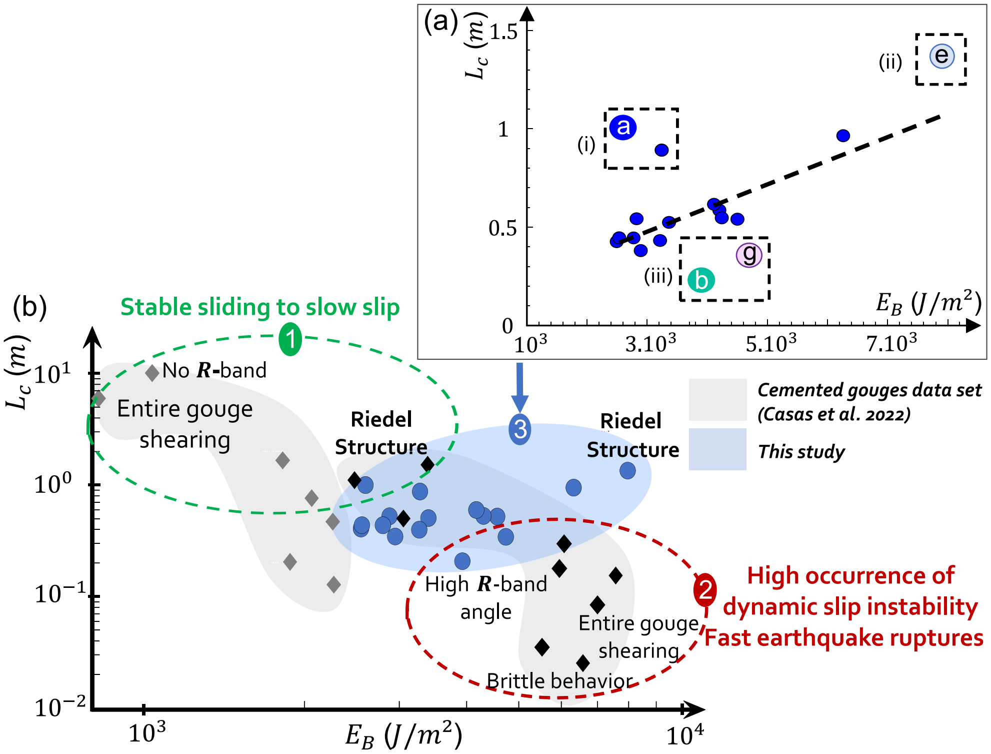

Figure 13. (a) Evolution of the critical nucleation length L_c (m) as a function of the breakdown energy E_B (J/m^2) for all the samples simulations, linear scale. (b) A larger picture of the L_c (m) as a function of E_B (J/m^2), log-scale, with results from (Casas et al., 2022) on cemented fault gouges with a variation of the percentage of cement for both dense (dark gray markers) and mid-dense samples (light gray markers). Matrix fault gouges of the present study are colored in blue. The choice was made to compare all the results using the same Young modulus and Poisson coefficient in Eq. (3) as if the same fault rock material was compared. Medium values for granite material are considered, $E \sim 60$ GPa, and $\nu = 0.3$, with an approximate $K_{\text{mean}} \sim 900$ GPa/m (considering the 20 mm—length gouge). All these results come from numerical experiments.

The comparison of these results with previous studies on cemented fault gouges from (Casas et al., 2022) in the same Figure 13b provides a more comprehensive view of the behavior of fault gouges. Both initial porosity and initial percentage of cementation influence gouge weakening and slip behaviors, playing a role in the gouge strength (brittleness, cohesion) and granular flow (particles agglomerates, *R*-bands). While the evolution of L_c with respect to E_G of matrix gouges is rather linear, the behavior of cemented gouges evolves in two steps depending on the initial porosity in the sample and the percentage of cement initially present in the numerical fault gouges. It is indeed clear from these revisited results that an increased porosity decreases E_B, and that an increased cementation decreases L_c.

1. Fault gouges with high L_c ($\gg 1$ m) and low E_B ($\ll 3.10^3$ J/m^2), (green zone 1), correspond to loose materials, fault gouges with no or very few infill materials (cement), or small inter-particle friction. They present a low friction peak and weakening rate. These materials are close to those defined as weak gouge materials (Bedford et al., 2022; Collettini et al., 2019; Orellana et al., 2018) with a less brittle behavior that tends to increase both the critical slip distance and the critical nucleation length. Greater mobility is thus allowed within the fault, and the associated breakdown energy remains low. They may lead to stable sliding or slow slip in the fault zone: very low shear modulus combined with large regions of nucleation is more likely to tend toward slow slip nucleation (Leeman et al., 2016; Scuderi et al., 2020). Regarding rheology, low cemented materials follow a ductile behavior without observation of apparent *R*-bands, inhibited by a critical dilation higher than 1%, may the tested samples be dense and mid-dense. Their behavior is close to fault gouges with small interparticle friction presenting a Riedel structure with a very low *R*-band angle orientation.
2. A second domain, with low L_c ($\ll 0.5$ m) and high E_B ($\gg 3.10^3$ J/m^2), (red zone 2), gathers both dense and highly cemented fault gouges and matrix fault gouges from the zone (iii) previously described with high interparticle friction or shear modulus. They present a high friction peak and a high weakening rate. However,

10.1029/2022JB025666

for these materials, the observed stress drop is much larger and also steeper (sharp, short, and intense peak), which means that if the shear stress peak is reached, the observed slip is more likely to occur in an unstable manner and with high energy release. The nucleation length decreases with an increase in cementation or interparticle friction, confirming that not much mobility is allowed within the system before the onset of dynamic instability. R-bands are significantly affected by a change in contact laws between particles (cohesion or friction) occurring with cement breakage. They appear for dense materials when a threshold of cementation is reached and are directly linked to the importance of the dilation phase, since the majority of the gouge remains cemented even after the weakening phase (Caniven et al., 2021; Casas, 2022). Cementation and high interparticle friction play a major role in the triggering of instabilities and perhaps also in fast earthquake rupture behaviors.

It is clear from this picture that both internal characteristics of the fault gouge and infill materials have a very important role in the occurrence of dynamic slip instability, and this observation gives new considerations to the study of the different classes of slow earthquakes and fast earthquake rupture (Bürgmann, 2018; Im et al., 2020; Leeman et al., 2015; Passelègue et al., 2019). There is an evident link between mechanics (friction) and energy-related quantities such as L_c and E_G, but the link between R-bands and dynamic instability occurrence is still unclear. (Moore et al., 1989) found in their experiments that the greatest stick-slip motion was observed for samples where: (a) strain is localized in well-developed shears combined with (b) some Riedel shears oriented at a relatively high angle. It leads to the conclusion that dense and highly cemented materials (clearly showing well-formed shear localizations, Y-band and R-band) are more likely to generate unstable behaviors, while mid-dense or dense materials with very low cementation (with no pronounced shear localizations) will rather tend toward a ductile, and stable behavior. Moreover, an increase in Riedel angle orientation, as for an increase in interparticle friction, could also be an indicator of unstable behaviors. However, these results are expected to be different from other fault gouge materials (Moore et al., 1989), such as clay minerals. The next objective will be to link the presence of a Riedel structure or R'-bands to a characteristic increase or decrease of critical nucleation length and breakdown energy.

4.3. Numerical Versus Laboratory Experiments: Limitations and Capabilities

Comparing numerical results with laboratory ones is not straightforward: the boundary conditions are different, and certain assumptions are made to allow the calculation to be carried out, sometimes leading to different physical phenomena. It is therefore important to clearly distinguish the phenomena involved in both cases. This section comes back to some key points regarding the model assumptions and the comparison with laboratory experiments.

The friction weakening observed in our simulations is due to the development of localized Y-bands, which unlock the dense granular assembly and allow shearing at lower shear stress levels. As observed, the friction drop associated with this weakening can be quite large, $\Delta\mu^* = \mu_p^* - \mu_{ss}^* \approx 0.3 \rightarrow 0.89$ (Table S4 in Supporting Information S1, Figures 4 and 6). However, in constant-velocity laboratory studies with a similar development of shear localization in granular gouges, no such stress drop is observed, and the friction coefficient remains relatively constant throughout the development of localized shear bands at macro-scale (Bedford & Faulkner, 2021; Gu & Wong, 1994; Scuderi et al., 2017, among others). The discrepancy between our numerical results and what is commonly observed in laboratory studies is due to a change in: (a) initial porosity, as a first-order influence, (b) contact stiffnesses (Figure 6), (c) and friction (Figure 4), as second-order variations. The initial porosity of our numerical samples is very low (<1%) whereas starting porosities in experimental studies are typically much higher (<20 %), depending on the material (Crawford et al., 2008; Kenigsberg et al., 2019). This very low porosity in our models is a signature of over-consolidated materials, for which both the density and strength of the material increase with time under compaction (Morrow & Byerlee, 1989). In a way, the weakening observed in our numerical experiments is analogs to the breakage of low-porosity intact rocks, which mainly depends on the strength of the dominant mineral (Dunn et al., 1973). However, the initial apparent cohesion in our numerical samples is equal to 6.4 MPa (in the sense of Mohr-Coulomb), which is more than quartz sand, but less than typical intact rock cohesion (Figure S2 in Supporting Information S1). On the other hand, fault gouge materials used in laboratory experiments are powders and sands, mainly under-consolidated and poorly cohesive (Sammis & Biegel, 1989; Schellart, 2000). The reality of fault gouges should be in between, not as dense (and cohesive) as these numerical experiments, but not as unconsolidated as synthetic fault gouges used in laboratories.

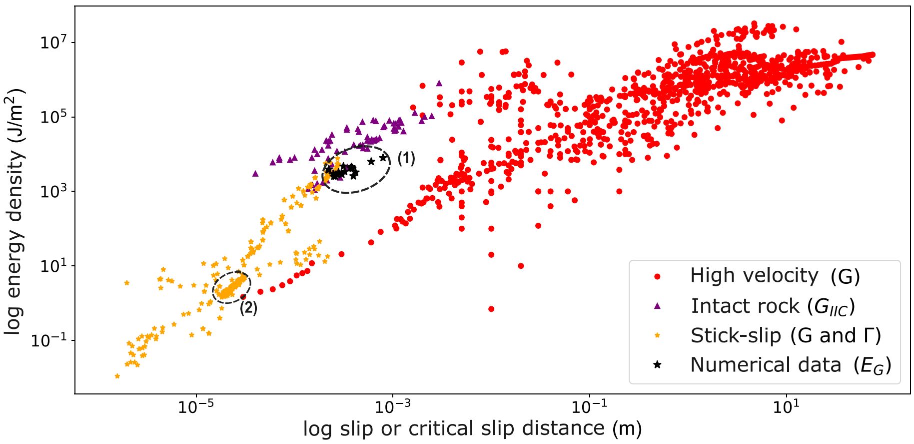

Figure 14. Fracture and breakdown energy data (J/m^2) from laboratory experiments and numerical data as a function of the slip or critical slip distance (m). This figure is modified from Cocco et al. (2023), and laboratory datasets can be downloaded at https://doi.org/10.5281/zenodo.6833943. Colors represent distinct datasets (change in the type of energy density and experimental configuration): estimates of the fracture energy G (red) by Aretusini et al. (2021), Boulton et al. (2017), Boutareaud et al. (2012),Brantut et al. (2008), Chen et al. (2017), Cornelio et al. (2019, 2020), de Paola et al. (2011), di Toro et al. (2006, 2011), Faulkner et al. (2011), Han et al. (2007, 2010), Harbord et al. (2021), Hirose and Bystricky (2007), Hou et al. (2012), Mizoguchi et al. (2007), Nielsen et al. (2008, 2016), Oohashi et al. (2015), Passelègue, Spagnuolo, et al. (2016), Rempe et al. (2017), Sawai et al. (2012, 2014), Seyler et al. (2020), Smith et al. (2013), Togo et al. (2011, 2016); Togo and Shimamoto (2012); Ujiie et al. (2013), Vannucchi et al. (2017), Violay et al. (2013, 2014), and Yao et al. (2013); shear fracture energy G_{IIc} (purple) by Aben et al. (2019, 2020), Hakami and Stephansson (1990), Zhang and Rummel (1990), Lockner et al. (1991), Moore and Lockner (1995), Ohnaka (2003), Ohnaka et al. (1997), Rummel et al. (1978), Wawersik and Brace (1971), Wong, (1982); estimates of fracture energy G and stick-slip energy density (orange) by Ohnaka (2003), Okubo and Dieterich (1981, 1984), Paglialunga et al. (2022), Passelègue, Schubnel, et al. (2016), Scuderi et al. (2020), Kammer and McLaskey (2019), C. Ke et al. (2018); breakdown energy E_B of numerical experiments (black). Zone (1) shows the numerical data set from this paper and zone (2) presents the data set of Scuderi et al. (2020) partly realized on quartz gouges.

Another explanation for the discrepancy observed in friction drop between laboratory and numerical experiments could be the absence of fragmentation in this DEM model. In laboratory experiments, there is an important wear rate at the beginning of the shearing, due to the comminution of particles (Scholz, 2019). During this important fragmentation, micromechanical models of failure have shown that intragranular failures (within grains) became predominant on intergranular failure (between grains), meaning that the energy is spent first to break particles before trying to make them move and localizing shearing (McBeck et al., 2019). This behavior also induces overall compaction at the beginning of the experiment (Gu & Wong, 1994). While in our model, the absence of fragmentation means that only intergranular failure happens, increasing shear stress, and dilation at the beginning of shearing.

Fragmentation and evolution of porosity are important mechanisms in the formation of shear localization and R-bands. But even though we don't take into account fragmentation, and don't show the same porosity as unconsolidated gouge used in laboratory experiments, R-bands appear with shearing, following closely the stages commonly observed in natural faults (Y. Katz et al., 2004) or in laboratory fault gouges (Bedford & Faulkner, 2021; Marone & Scholz, 1989; Scuderi et al., 2017; Smith et al., 2015). These laboratory experiments suggested that grain size reduction helps control localization behavior, and instabilities (Bedford & Faulkner, 2021), but according to our numerical simulations, localization patterns can also appear without grain size reduction, and are controlled by a change in porosity. Indeed, fabrics and shear bands compete with initial compaction (i.e., initial porosity) as the dominant control on elastic and frictional properties (Kenigsberg et al., 2019). This phenomenon could explain why, even with different initial porosity, once the R-bands and B-bands start to be activated, they control the elastic and frictional properties of the fault.

Recent laboratory experiments showed that the effect of temperature on internal friction cannot be neglected because it influences the weakening behavior of the fault (Aubry et al., 2018; Cornelio et al., 2022; Nielsen et al., 2021). However, in these experiments, it is not possible to distinguish the thermal effect from the microstructural effect in the recorded shear stress value because they are mixed. In our work, we investigate the effect of slip in the texture development effect (a) in the friction curve μ^*, (b) on the breakdown energy E_B, neglecting temperature increase

10.1029/2022JB025666

(first-order friction changes). Without taking into account this thermal effect on friction, the steady-state friction μ^*_{ss} is quite high (Figures 4a and 6a and 6b). Indeed, the breakdown energy observed in our model can be framed as mechanical energy in absence of thermal weakening, which is the contribution of: dilation energy (strain localization and fabric development during shearing) and frictional energy (contact interaction and friction between particles). Figure 14 shows the evolution of breakdown and fracture energy as a function of slip for laboratory experiments, from (Cocco et al., 2023), where we added our breakdown energy for numerical samples, Figure 14. Even if it is not straightforward to compare with laboratory data sets, our breakdown energy data highlighted in zone (a), perfectly fit within the range explored in laboratory experiments and are consistent with the scaling between energy and slip (Cocco et al., 2023). We can notice that the energy released by the numerical gouge samples is in between the shear fracture energy G_{IIc} computed on intact rock experiments (purple) and the fracture energy G computed for stick-slip experiments (orange). Our numerical results are consistent with stick-slip experiments since the evolution of temperature can be somehow neglected in these types of experiments (low sliding velocity). Once again, the numerical gouge behavior is in between laboratory experiments on intact rocks and gouge materials, Figure 14. We also highlighted experiments from (Scuderi et al., 2020), zone (2), where the energy is calculated for quartz gouge experiments (similar material). The difference observed can be due to the change in boundary conditions and normal stress applied, the discrepancies in physical phenomenon highlighted in the previous statements, but also to the fact that they are measuring energy from velocity steps, whereas we are measuring the overall energy dissipated by the fault gouge.

Recently temperature control has been instrumented in the DEM software MELODY, allowing to follow temperature evolution during sliding by temperature increment in grains (Mollon et al., 2021). To properly take into account the effect of temperature in our model, it would also be necessary to observe a change in the behavior of the material at the local scale, which is not yet implemented. However, the results that we have shown make it possible to link the parameters of the properties at the grain scale with the kinematics behavior of the sheared material in a quasi-static regime. These results are very important input parameters for larger-scale dynamic models.

The numerical experiments also show that despite the different boundary conditions and hypothesis used, formation but also de-activation of R-bands (Figure 3) appear with shearing as found in laboratory experiments between yielding and the onset of stick-slip and, at the end of stick-slip (Bedford & Faulkner, 2021). Meaning that the R-bands observed at larger scales in exhumed faults may only be a 'visible' part of the deformations that have occurred during the life of a sheared fault.

5. Conclusions

A set of 2D-DEM simulations was performed with numerical fault gouges composed of a very dense assembly of polygonal-shaped particles. The first aim was to explore the link between grain-scale gouge characteristics and fault gouge kinematics with shear band formation during friction weakening. It was found that a small change in gouge characteristics such as the interparticle friction, gouge shear modulus or the number of particles within the gouge thickness impacts R-band formation through their orientation angle and the type of Riedel structure formed. Moreover, in order to observe any shear localization in fault gouges, they must be mature enough to have a sufficiently thick and comminuted gouge to allow R-band localization.

Then it appears that, even for similar rheological behaviors, different consequences can be observed on breakdown energy and the occurrence of dynamic slip instabilities. Fault gouges with low interparticle friction, (or with no or very few cementation), allow greater mobility within the fault and give low breakdown energy. They also present a decrease in the orientation angle of R-bands assumed to be characteristic of a more stable fault gouge. These materials lead to rather ductile behavior with low friction peak and weakening rate (weak gouge) and are expected to lead to a rather stable sliding or slow slip. On the contrary, materials with high interparticle friction or high bulk shear modulus, (or dense and highly cemented fault gouges), are less compliant materials. Not much slip is needed before going into dynamic slip instabilities, and high breakdown energy is observed. They present a high friction peak and a high weakening rate, which is prone to switch the fault behavior from a ductile aseismic response to a brittle seismic slip and increase fast earthquake rupture. Discrepancies with typical shearing experiments on crushed rocks used as synthetic gouges are attributed to large differences in the initial state of the granular sample, specifically its porosity. While the porosity used in our simulations corresponds to an extremely over-consolidated material, we postulate that typical laboratory samples may be looser than actual fault gouge, and suggest including an over-consolidation ratio as a control parameter in future experiments.

This study reinforces our convictions about the importance of R-bands within the fault, and the need to understand their link with the occurrence of dynamic slip instabilities. In the next step, we will focus on an energetic method to link the behavior of each band of deformation with the friction observed in the gouge.

Conflict of Interest

The authors declare no conflicts of interest relevant to this study.

Data Availability Statement

All simulations were performed with the open-source software MELODY version 3.94 (https://doi.org/10.5281/zenodo.4305614) developed by the second author and described in Mollon (2018). Simulation results can be found in Casas (2022), "Influence of grain-scale properties on localization patterns and slip weakening within dense granular fault gouges", Mendeley Data, V1, https://doi.org/10.17632/pphkhf72r5.1. Other explanations are included in the Supporting Information file or are available by contacting the corresponding author.

Acknowledgments
This study was funded by INSA Lyon, through a national Ph.D. grant led by A. Daouadji and G. Mollon. We thank Chiara Cornelio, a second reviewer, and the Associate Editor Michael Heap whose comments and corrections helped strengthen this manuscript.

References

Aben, F. M., Brantut, N., & Mitchell, T. M. (2020). Off-fault damage characterization during and after experimental quasi-static and dynamic rupture in crustal rock from laboratory P wave tomography and microstructures. *Journal of Geophysical Research: Solid Earth*, *125*(8). https://doi.org/10.1029/2020JB019860

Aben, F. M., Brantut, N., Mitchell, T. M., & David, E. C. (2019). Rupture energetics in crustal rock from laboratory-scale seismic tomography. *Geophysical Research Letters*, *46*(13), 7337–7344. https://doi.org/10.1029/2019GL083040

Abercrombie, R. E., & Rice, J. R. (2005). Can observations of earthquake scaling constrain slip weakening. *Geophysical Journal International*, *162*(2), 406–424. https://doi.org/10.1111/j.1365-246X.2005.02579.x

Aharonov, E., & Sparks, D. (2004). Stick-slip motion in simulated granular layers. *Journal of Geophysical Research*, *109*(9), 1–12. https://doi.org/10.1029/2003JB002597

Anthony, J. L., & Marone, C. (2005). Influence of particle characteristics on granular friction. *Journal of Geophysical Research*, *110*(8), 1–14. https://doi.org/10.1029/2004JB003399

Aretusini, S., Meneghini, F., Spagnuolo, E., Harbord, C. W., & di Toro, G. (2021). Fluid pressurisation and earthquake propagation in the Hikurangi subduction zone. *Nature Communications*, *12*(1), 2481. https://doi.org/10.1038/s41467-021-22805-w

Aubry, J., Passelègue, F. X., Deldicque, D., Girault, F., Marty, S., Lahfid, A., et al. (2018). Frictional heating processes and energy budget during laboratory earthquakes. *Geophysical Research Letters*, *45*(22), 12274–12282. https://doi.org/10.1029/2018GL079263

Bedford, J. D., & Faulkner, D. R. (2021). The role of grain size and effective normal stress on localization and the frictional stability of simulated quartz gouge. *Geophysical Research Letters*, *48*(7). https://doi.org/10.1029/2020GL092023

Bedford, J. D., Faulkner, D. R., & Lapusta, N. (2022). Fault rock heterogeneity can produce fault weakness and reduce fault stability. *Nature Communications*, *13*(1), 1–7. https://doi.org/10.1038/s41467-022-27998-2

Beeler, N. M., Tullis, T. E., Blanpied, M. L., & Weeks, J. D. (1996). Frictional behavior of large displacement experimental faults. *Journal of Geophysical Research B: Solid Earth*, *101*(4), 8697–8715. https://doi.org/10.1029/96jb00411

Biegel, R. L., Sammis, C. G., & Dieterich, J. H. (1989). The frictional properties of a simulated gouge having a fractal particle distribution. *Journal of Structural Geology*, *11*(7), 827–846. https://doi.org/10.1016/0191-8141(89)90101-6

Bolotskaya, E., & Hager, B. H. (2022). A 1D spring-slider model with a simple poly-linear failure law produces rich variations in slip behavior. *Bulletin of the Seismological Society of America*, *112*(6), 2795–2811. 1–17. https://doi.org/10.1785/0120220052

Boulton, C., Yao, L., Faulkner, D. R., Townend, J., Toy, V. G., Sutherland, R., et al. (2017). High-velocity frictional properties of Alpine Fault rocks: Mechanical data, microstructural analysis, and implications for rupture propagation. *Journal of Structural Geology*, *97*, 71–92. https://doi.org/10.1016/j.jsg.2017.02.003

Boutareaud, S., Hirose, T., Andréani, M., Pec, M., Calugaru, D. G., Boullier, A. M., & Doan, M. L. (2012). On the role of phyllosilicates on fault lubrication: Insight from micro-and nanostructural investigations on talc friction experiments. *Journal of Geophysical Research*, *117*(8). https://doi.org/10.1029/2011JB009006

Brantut, N., Schubnel, A., Rouzaud, J.-N., Brunet, F., & Shimamoto, T. (2008). High-velocity frictional properties of a clay-bearing fault gouge and implications for earthquake mechanics. *Journal of Geophysical Research*, *113*(B10), B10401. https://doi.org/10.1029/2007JB005551

Bürgmann, R. (2018). The geophysics, geology and mechanics of slow fault slip. *Earth and Planetary Science Letters*, *495*, 112–134. https://doi.org/10.1016/j.epsl.2018.04.062

Bürgmann, R., & Dresen, G. (2008). Rheology of the lower crust and upper mantle: Evidence from rock mechanics, geodesy, and field observations. *Annual Review of Earth and Planetary Sciences*, *36*(1), 531–567. https://doi.org/10.1146/annurev.earth.36.031207.124326

Byerlee, J. D. (1978). Friction of rocks. *Pure and Applied Geophysics*, *116*(4–5), 615–626. https://doi.org/10.1007/BF00876528

Byerlee, J. D., & Brace, W. F. (1968). Stick slip, stable sliding, and earthquakes-Effect of rock type, pressure, strain rate, and stiffness. *Journal of Geophysical Research*, *73*(18), 6031–6037. https://doi.org/10.1029/JB073i018p06031

Byerlee, J. D., Mjachkin, V., Summers, R., & Voevoda, O. (1978). Structures developed sliding and stick-slip in fault gouge during stable. *Tectonophysics*, *44*(1–4), 161–171. https://doi.org/10.1016/0040-1951(78)90068-9

Campillo, M., & Ionescu, I. R. (1997). Initiation of antiplane shear instability under slip dependent friction. *Journal of Fluid Mechanics*, *102*(B9), 363–371. https://doi.org/10.1029/97JB01508

Caniven, Y., Morgan, J. K., & Blank, D. G. (2021). The role of along-fault dilatancy in fault slip behavior. *Journal of Geophysical Research: Solid Earth*, *126*(11), 1–21. https://doi.org/10.1029/2021JB022310

Casas, N. (2022). *Insights on the behavior of fault gouges during seismic sliding: A numerical investigation from granular rheology to friction laws*. INSA Lyon.

Casas, N., Mollon, G., & Daouadji, A. (2021). Shear bands in dense fault gouge. *EPJ Web of Conferences - Powders and Grains*, *249*, 1–4. https://doi.org/10.1051/epjconf/202124911006

Casas, N., Mollon, G., & Daouadji, A. (2022). DEM analyses of cemented Granular Fault Gouges at the onset of seismic sliding: Peak strength, development of shear zones and kinematics. *Pure and Applied Geophysics*, *179*(2), 679–707. https://doi.org/10.1007/s00024-021-02934-5

Chen, J., Niemeijer, A. R., & Fokker, P. A. (2017). Vaporization of fault water during seismic slip. *Journal of Geophysical Research: Solid Earth*, *122*(6), 4237–4276. https://doi.org/10.1002/2016JB013824

Cho, N., Martin, C. D., & Sego, D. C. (2008). Development of a shear zone in brittle rock subjected to direct shear. *International Journal of Rock Mechanics and Mining Sciences*, *45*(8), 1335–1346. https://doi.org/10.1016/j.ijrmms.2008.01.019

Cocco, M., Aretusini, S., Cornelio, C., Nielsen, S. B., Spagnuolo, E., Tinti, E., et al. (2023). Fracture energy and breakdown work during earthquakes. https://doi.org/10.1146/annurev-earth-071822

Collettini, C., Tesei, T., Scuderi, M. M., Carpenter, B. M., & Viti, C. (2019). Beyond Byerlee friction, weak faults and implications for slip behavior. *Earth and Planetary Science Letters*, *519*, 245–263. https://doi.org/10.1016/j.epsl.2019.05.011

Cornelio, C., Passelègue, F. X., Spagnuolo, E., di Toro, G., & Violay, M. (2020). Effect of fluid viscosity on fault reactivation and coseismic weakening. *Journal of Geophysical Research: Solid Earth*, *125*(1). https://doi.org/10.1029/2019JB018883

Cornelio, C., Spagnuolo, E., Aretusini, S., Nielsen, S., Passelègue, F., Violay, M., et al. (2022). Determination of parameters characteristic of dynamic weakening mechanisms during seismic faulting in cohesive rocks. *Journal of Geophysical Research: Solid Earth*, *127*(7), 1–23. https://doi.org/10.1029/2022JB024356

Cornelio, C., Spagnuolo, E., di Toro, G., Nielsen, S., & Violay, M. (2019). Mechanical behaviour of fluid-lubricated faults. *Nature Communications*, *10*(1), 1274. https://doi.org/10.1038/s41467-019-09293-9

Crawford, B. R., Faulkner, D. R., & Rutter, E. H. (2008). Strength, porosity, and permeability development during hydrostatic and shear loading of synthetic quartz-clay fault gouge. *Journal of Geophysical Research*, *113*(3), B03207. https://doi.org/10.1029/2006JB004634

Cundall, P. A., & Strack, O. D. L. (1979). A discrete numerical model for granular assemblies. *Géotechnique*, *29*(1), 47–65. https://doi.org/10.1680/geot.1979.29.1.47

Da Cruz, F., Emam, S., Prochnow, M., Roux, J. N., & Chevoir, F. (2005). Rheophysics of dense granular materials: Discrete simulation of plane shear flows. *Physical Review*, *72*(2), 1–17. https://doi.org/10.1103/PhysRevE.72.021309

Davis, G. H., Bump, A. P., García, P. E., & Ahlgren, S. G. (2000). Conjugate Riedel deformation band shear zones. *Journal of Structural Geology*, *22*(2), 169–190. https://doi.org/10.1016/S0191-8141(99)00140-6

de Paola, N., Hirose, T., Mitchell, T., di Toro, G., Viti, C., & Shimamoto, T. (2011). Fault lubrication and earthquake propagation in thermally unstable rocks. *Geology*, *39*(1), 35–38. https://doi.org/10.1130/G31398.1

Dieterich, J. H. (1972). Time-dependent friction in rocks. *Journal of Geophysical Research*, *77*(20), 3690–3697. https://doi.org/10.1029/jb077i020p03690

Dieterich, J. H. (1979). Modeling of rock friction experimental results and constitutive equations. *Journal of Geophysical Research*, *84*(9), 2161–2168. https://doi.org/10.1029/jb084ib05p02161

di Toro, G., Han, R., Hirose, T., de Paola, N., Nielsen, S., Mizoguchi, K., et al. (2011). Fault lubrication during earthquakes. *Nature*, *471*(7339), 494–498. https://doi.org/10.1038/nature09838

di Toro, G., Hirose, T., Nielsen, S., Pennacchioni, G., & Shimamoto, T. (2006). Natural and experimental evidence of melt lubrication of faults during earthquakes. *Science*, *311*(5761), 647–649. https://doi.org/10.1126/science.1121012

Di Toro, G., Pennacchioni, G., & Nielsen, S. (2009). Pseudotachylytes and earthquake source mechanics. *International Geophysics*, *94*(C), 87–133. https://doi.org/10.1016/S0074-6142(08)00005-3

Dorostkar, O., & Carmeliet, J. (2019). Grain friction controls characteristics of seismic cycle in faults with granular gouge journal of geophysical research: Solid Earth. *Journal of Geophysical Research B: Solid Earth*, *124*(7), 6475–6489. https://doi.org/10.1029/2019JB017374

Dorostkar, O., Guyer, R. A., Johnson, P. A., Marone, C., & Carmeliet, J. (2017a). On the micromechanics of slip events in sheared, fluid-saturated fault gouge. *Geophysical Research Letters*, *44*(12), 6101–6108. https://doi.org/10.1002/2017GL073768

Dorostkar, O., Guyer, R. A., Johnson, P. A., Marone, C., & Carmeliet, J. (2017b). On the role of fluids in stick-slip dynamics of saturated granular fault gouge using a coupled computational fluid dynamics-discrete element approach. *Journal of Geophysical Research: Solid Earth*, *122*(5), 3689–3700. https://doi.org/10.1002/2017JB014099

Dorostkar, O., Guyer, R. A., Johnson, P. A., Marone, C., & Carmeliet, J. (2018). Cohesion-induced stabilization in stick-slip dynamics of weakly wet, sheared Granular Fault gouge. *Journal of Geophysical Research: Solid Earth*, *123*(3), 2115–2126. https://doi.org/10.1002/2017JB015171

Dunn, D. E., LaFountain, L. J., & Jackson, R. E. (1973). Porosity dependence and mechanism of brittle fracture in sandstones. *Journal of Geophysical Research*, *78*(14), 2403–2417. https://doi.org/10.1029/jb078i014p02403

Faulkner, D. R., Mitchell, T. M., Behnsen, J., Hirose, T., & Shimamoto, T. (2011). Stuck in the mud? Earthquake nucleation and propagation through accretionary forearcs. *Geophysical Research Letters*, *38*(18). https://doi.org/10.1029/2011GL048552

Ferdowsi, B., Griffa, M., Guyer, R. A., Johnson, P. A., Marone, C., & Carmeliet, J. (2014). Three-dimensional discrete element modeling of triggered slip in sheared granular media. *Physical Review*, *89*(4), 1–12. https://doi.org/10.1103/PhysRevE.89.042204

Ferdowsi, B., & Rubin, A. M. (2020). A granular physics-based view of fault friction experiments. 1–32. https://doi.org/10.1029/2019JB019016

Ferri, F., Toro, G. D., Hirose, T., Han, R., Noda, H., Shimamoto, T., et al. (2011). *Low- to high- velocity frictional properties of the clay-rich gouges from the slipping zone of the 1963 Vaiont slide, northern Italy*, *116*, 1–17. https://doi.org/10.1029/2011JB008338

Fialko, Y. (2007). Fracture and frictional mechanics - Theory. *Treatise on Geophysics*, *4*, 83–106. https://doi.org/10.1016/B978-044452748-6.00062-6

Fondriest, M., Mecklenburgh, J., Passelegue, F. X., Artioli, G., Nestola, F., Spagnuolo, E., et al. (2020). Pseudotachylyte alteration and the rapid fade of earthquake scars from the geological record. *Geophysical Research Letters*, *47*(22), 1–9. https://doi.org/10.1029/2020GL090020

Gao, K., Euser, B. J., Rougier, E., Guyer, R. A., Lei, Z., Knight, E. E., et al. (2018). Modeling of stick-slip behavior in sheared Granular Fault gouge using the combined finite-discrete element method. *Journal of Geophysical Research: Solid Earth*, *123*(7), 5774–5792. https://doi.org/10.1029/2018JB015668

Giorgetti, C., Tesei, T., Scuderi, M. M., & Collettini, C. (2019). Experimental insights into fault reactivation in gouge - filled fault zones. *Journal of Geophysical Research: Solid Earth*, *124*(4), 4189–4204. https://doi.org/10.1029/2018JB016813

Griffith, A. (1924). The theory of rupture. *First International Congress for Applied Mechanics*, (pp. 55–63).

Gu, Y., & Wong, T.-F. (1994). Development of shear localization in simulated quartz gouge: Effect of cumulative slip and gouge particle size. *PAGEOPH*, *143*(3), 387–423. https://doi.org/10.1007/bf00874336

Guo, Y., & Morgan, J. K. (2004). Influence of normal stress and grain shape on granular friction: Results of discrete element simulations. *Journal of Geophysical Research*, *109*(B12), B12305. https://doi.org/10.1029/2004JB003044

Hadizadeh, J., Tullis, T. E., White, J. C., & Konkachbaev, A. I. (2015). Shear localization, velocity weakening behavior, and development of cataclastic foliation in experimental granite gouge. *Journal of Structural Geology*, *71*, 86–99. https://doi.org/10.1016/j.jsg.2014.10.013

Haines, S. H., Kaproth, B., Marone, C., Saffer, D., & Van der Pluijm, B. (2013). Shear zones in clay-rich fault gouge: A laboratory study of fabric development and evolution. *Journal of Structural Geology*, *51*, 206–225. https://doi.org/10.1016/j.jsg.2013.01.002

Hakami, H., & Stephansson, O. (1990). Shear fracture energy of Stripa granite-results of controlled triaxial testing. *Engineering Fracture Mechanics*, *35*(4–5), 855–865. https://doi.org/10.1016/0013-7944(90)90170-L

Han, R., Hirose, T., & Shimamoto, T. (2010). Strong velocity weakening and powder lubrication of simulated carbonate faults at seismic slip rates. *Journal of Geophysical Research*, *115*(B3), B03412. https://doi.org/10.1029/2008JB006136

Han, R., Shimamoto, T., Hirose, T., Ree, J.-H., & Ando, J. (2007). Ultralow friction of carbonate faults caused by thermal decomposition. *Science*, *316*(5826), 878–881. https://doi.org/10.1126/science.1139763

Harbord, C., Brantut, N., Spagnuolo, E., & di Toro, G. (2021). Fault friction during simulated seismic slip pulses. *Journal of Geophysical Research: Solid Earth*, *126*(8). https://doi.org/10.1029/2021JB022149

Hirose, T., & Bystricky, M. (2007). Extreme dynamic weakening of faults during dehydration by coseismic shear heating. *Geophysical Research Letters*, *34*(14), L14311. https://doi.org/10.1029/2007GL030049

Hou, L., Ma, S., Shimamoto, T., Chen, J., Yao, L., Yang, X., & Okimura, Y. (2012). Internal structures and high-velocity frictional properties of a bedding-parallel carbonate fault at Xiaojiaqiao outcrop activated by the 2008 Wenchuan earthquake. *Earthquake Science*, *25*(3), 197–217. https://doi.org/10.1007/s11589-012-0846-2

Im, K., Marone, C., & Elsworth, D. (2019). The transition from steady frictional sliding to inertia-dominated instability with rate and state friction. *Journal of the Mechanics and Physics of Solids*, *122*, 116–125. https://doi.org/10.1016/j.jmps.2018.08.026

Im, K., Saffer, D., Marone, C., & Avouac, J. P. (2020). Slip-rate-dependent friction as a universal mechanism for slow slip events. *Nature Geoscience*, *13*(10), 705–710. https://doi.org/10.1038/s41561-020-0627-9

Jiao, L., Klinger, Y., & Scholtès, L. (2021). Fault segmentation pattern controlled by thickness of brittle crust. *Geophysical Research Letters*, *48*(19), 1–7. https://doi.org/10.1029/2021GL093390

Kaminskaite, I., Fisher, Q. J., & Michie, E. A. H. (2019). Microstructure and petrophysical properties of deformation bands in high porosity carbonates. *Journal of Structural Geology*, *119*(December 2018), 61–80. https://doi.org/10.1016/j.jsg.2018.12.001

Kammer, D. S., & McLaskey, G. C. (2019). Fracture energy estimates from large-scale laboratory earthquakes. *Earth and Planetary Science Letters*, *511*, 36–43. https://doi.org/10.1016/j.epsl.2019.01.031

Kanamori, H., & Heaton, T. H. (2000). Microscopic and macroscopic physics of earthquakes. In J. B. Rundle, D. L. Turcotte, & W. Klein (Eds.), *Geocomplexity and the physics of earthquakes* (pp. 147–163). https://doi.org/10.1029/GM120p0147

Kasyap, S., & Senetakis, K. (2021). Micromechanical-based experimental and analytical studies on rate effects and stick-slip instability of smooth quartz surfaces in the presence of plastic and non-plastic gouges. *International Journal for Numerical and Analytical Methods in Geomechanics*, *45*(6), 776–793. https://doi.org/10.1002/nag.3178

Katz, R., Spiegelman, M., & Holtzman, B. (2006). The dynamics of melt and shear localization in partially molten aggregates. *Nature Letters*, *442*(August), 2–5. https://doi.org/10.1038/nature05039

Katz, Y., & Weinberger, R. (2005). Strain localization in sandstone during embryonic stages of shear-zone evolution. *Terra Nova*, *17*(4), 311–316. https://doi.org/10.1111/j.1365-3121.2005.00615.x

Katz, Y., Weinberger, R., & Aydin, A. (2004). Geometry and kinematic evolution of Riedel shear structures, Capitol Reef National Park, Utah. *Journal of Structural Geology*, *26*(3), 491–501. https://doi.org/10.1016/j.jsg.2003.08.003

Ke, C., McLaskey, G. C., & Kammer, D. S. (2018). Rupture termination in laboratory-generated earthquakes. *Geophysical Research Letters*, *45*(23). https://doi.org/10.1029/2018GL080492

Ke, C. Y., McLaskey, G. C., & Kammer, D. S. (2022). Earthquake breakdown energy scaling despite constant fracture energy. *Nature Communications*, *13*(1), 1–8. https://doi.org/10.1038/s41467-022-28647-4

Kenigsberg, A. R., Rivière, J., Marone, C., & Saffer, D. M. (2019). The effects of shear strain, fabric, and porosity evolution on elastic and mechanical properties of clay-rich fault gouge. *Journal of Geophysical Research: Solid Earth*, *124*(11), 10968–10982. https://doi.org/10.1029/2019JB017944

Lambe, T. W., & Whitman, R. V. (1991). *Soil mechanics* (Vol. 10). John Wiley & Sons.

Lee, H. K., & Kim, H. S. (2005). Comparison of structural features of the fault zone developed at different protoliths: Crystalline rocks and mudrocks. *Journal of Structural Geology*, *27*(11), 2099–2112. https://doi.org/10.1016/j.jsg.2005.06.012

Leeman, J., Saffer, D., Scuderi, M., & Marone, C. (2016). Laboratory observations of slow earthquakes and the spectrum of tectonic fault slip modes. *Nature Communications*, *7*, 1–6. https://doi.org/10.1038/ncomms11104

Leeman, J., Scuderi, M. M., Marone, C., & Saffer, D. (2015). Stiffness evolution of granular layers and the origin of repetitive, slow, stick-slip frictional sliding. *Granular Matter*, *17*(4), 447–457. https://doi.org/10.1007/s10035-015-0565-1

Lefevre, M., Souloumiac, P., Cubas, N., & Klinger, Y. (2020). Experimental evidence for crustal control over seismic fault segmentation. *Geology*, *48*(8), 844–848. https://doi.org/10.1130/G47115.1

Lockner, D. A., & Beeler, N. M. (2002). Rock failure and earthquakes. *International Geophysics Series*, *81*(A), 505–538.

Lockner, D. A., Byerlee, J. D., Kuksenkot, V., Ponomarev, A., & Sidorin, A. (1991). Quasi-static fault growth and shear fracture energy in granite.

Logan, J. M., Dengo, C. A., Higgs, N. G., & Wang, Z. Z. (1992). Fabrics of experimental fault zones: Their development and relationship to mechanical behavior. *International Geophysics* (Vol. 51, pp. 33–67). Elsevier.

Lynch, J. C., & Richards, M. a. (2001). Finite element models of stress orientations in well-developed strike-slip fault zones: Implications for the distribution of lower crustal strain. *Journal of Geophysical Research*, *106*(B11), 26707–26729. https://doi.org/10.1029/2001JB000289

Lyu, Z., Rivière, J., Yang, Q., & Marone, C. (2019). On the mechanics of granular shear: The effect of normal stress and layer thickness on stick-slip properties. *Tectonophysics*, *763*(April), 86–99. https://doi.org/10.1016/j.tecto.2019.04.010

Mair, K., Frye, K. M., & Marone, C. (2002). Influence of grain characteristics on the friction of granular shear zones. *Journal of Geophysical Research*, *107*(B10), ECV4-1–ECV4-9. https://doi.org/10.1029/2001JB000516

Marone, C. (1998). Laboratory-derived friction laws and their application to seismic faulting. *Annual Review of Earth and Planetary Sciences*, *26*(1), 643–696. https://doi.org/10.1146/annurev.earth.26.1.643

Marone, C., & Saffer, D. M. (2015). The mechanics of frictional healing and slip instability during the seismic cycle. In *Treatise on geophysics* (2nd ed.4). Elsevier. https://doi.org/10.1016/B978-0-444-53802-4.00092-0

Marone, C., & Scholz, C. H. (1988). The depth of seismic faulting and the upper transition from stable to unstable slip regimes. *Geophysical Research Letters*, *15*(8), 621–624. https://doi.org/10.1029/GL015i006p00621

Marone, C., & Scholz, C. H. (1989). Particle-size distribution and microstructures within simulated fault gouge. *Journal of Structural Geology*, *11*(7), 799–814. https://doi.org/10.1016/0191-8141(89)90099-0

McBeck, J., Mair, K., & Renard, F. (2019). How porosity controls macroscopic failure via propagating fractures and percolating force chains in porous granular rocks. *Journal of Geophysical Research: Solid Earth*, *124*(9), 9920–9939. https://doi.org/10.1029/2019JB017825

McLaskey, G. C. (2019). Earthquake initiation from laboratory observations and implications for foreshocks. *Journal of Geophysical Research: Solid Earth*, *124*(12), 12882–12904. https://doi.org/10.1029/2019JB018363

Mizoguchi, K., Hirose, T., Shimamoto, T., & Fukuyama, E. (2007). Reconstruction of seismic faulting by high-velocity friction experiments: An example of the 1995 Kobe earthquake. *Geophysical Research Letters*, *34*(1), L01308. https://doi.org/10.1029/2006GL027931

Mollon, G. (2016). A multibody meshfree strategy for the simulation of highly deformable granular materials. *International Journal for Numerical Methods in Engineering*, *108*(12), 1477–1497. https://doi.org/10.1002/nme.5258

Mollon, G. (2018). A unified numerical framework for rigid and compliant granular materials. *Computational Particle Mechanics*, *5*(4), 517–527. https://doi.org/10.1007/s40571-018-0187-6

Mollon, G., Aubry, J., & Schubnel, A. (2021). Simulating melting in 2D seismic fault gouge. *Journal of Geophysical Research: Solid Earth*, *126*(6), 1–19. https://doi.org/10.1029/2020JB021485

Mollon, G., Quacquarelli, A., Andò, E., & Viggiani, G. (2020). Can friction replace roughness in the numerical simulation of granular materials? *Granular Matter*, *22*(42), 42. https://doi.org/10.1007/s10035-020-1004-5

Mollon, G., & Zhao, J. (2012). Fourier-Voronoi-based generation of realistic samples for discrete modelling of granular materials. *Granular Matter*, *5*, 621–638. https://doi.org/10.1007/s10035-012-0356-x

Moore, D. E., & Byerlee, J. D. (1992). Relationships between sliding behavior and internal geometry of laboratory fault zones and some creeping and locked strike-slip faults of California. *Tectonophysics*, *211*(1–4), 305–316. https://doi.org/10.1016/0040-1951(92)90067-G

Moore, D. E., & Lockner, D. A. (1995). The role of microcracking in shear-fracture propagation in granite. *Journal ofStrucrural Geology*, *17*(1).

Moore, D. E., Summers, R., & Byerlee, J. D. (1989). Sliding behavior and deformation textures of heated illite gouge. *Journal of Structural Geology*, *1*(3), 329–342. https://doi.org/10.1016/0191-8141(89)90072-2

Morgan, J. K. (1999). Numerical simulations of granular shear zones using the distinct element method: 2. Effects of particle size distribution and interparticle friction on mechanical behavior. *Journal of Geophysical Research*, *104*(B2), 2721–2732. https://doi.org/10.1029/1998jb900055

Morgan, J. K., & Boettcher, M. S. (1999). Numerical simulations of granular shear zones using the distinct element method: 1. Shear zone kinematics and the micromechanics of localization. *Journal of Geophysical Research*, *104*(B2), 2703–2719. https://doi.org/10.1029/1998jb900056

Morrow, C. A., & Byerlee, J. D. (1989). Experimental studies of compaction and dilatancy during frictional sliding on faults containing gouge. *Journal of Structural Geology*, *11*(7), 815–825. https://doi.org/10.1016/0191-8141(89)90100-4

Nielsen, S., Spagnuolo, E., Smith, S. A. F., Violay, M., di Toro, G., & Bistacchi, A. (2016). Scaling in natural and laboratory earthquakes. *Geophysical Research Letters*, *43*(4), 1504–1510. https://doi.org/10.1002/2015GL067490

Nielsen, S., Spagnuolo, E., Violay, M., & Di Toro, G. (2021). Thermal weakening friction during seismic slip: Experiments and models with heat sources and sinks. *Journal of Geophysical Research: Solid Earth*, *126*(5). https://doi.org/10.1029/2020JB020652

Nielsen, S., Toro, G. d., Hirose, T., & Shimamoto, T. (2008). Frictional melt and seismic slip. *Journal of Geophysical Research*, *113*(B1), 1308. https://doi.org/10.1029/2007JB005122

Niemeijer, A., Toro, G. D., Nielsen, S., & Felice, F. D. (2011). Frictional melting of gabbro under extreme experimental conditions of normal stress, acceleration, and sliding velocity. *Journal of Geophysical Research*, *116*, B07404. https://doi.org/10.1029/2010JB008181

Nouguier-Lehon, C., Cambou, B., & Vincens, E. (2003). Influence of particle shape and angularity on the behaviour of granular materials: A numerical analysis. *International Journal for Numerical and Analytical Methods in Geomechanics*, *27*(14), 1207–1226. https://doi.org/10.1002/nag.314

Ohnaka, M. (2003). A constitutive scaling law and a unified comprehension for frictional slip failure, shear fracture of intact rock, and earthquake rupture. *Journal of Geophysical Research*, *108*(B2). https://doi.org/10.1029/2000jb000123

Ohnaka, M. (2013). *The physics of rock failure and earthquakes*. Cambridge University Press. https://doi.org/10.1017/CBO9781139342865

Ohnaka, M., Akatsu, M., Mochizuki, H., Odedra, A., Tagashira, F., & Yamamoto, Y. (1997). A constitutive law for the shear failure of rock under lithospheric conditions. *Tectonophysics*, *277*(1–3), 1–27. https://doi.org/10.1016/S0040-1951(97)00075-9

Ohnaka, M., & Shen, L. (1999). Scaling of the shear rupture process from nucleation to dynamic propagation: Implications of geometric irregularity of the rupturing surfaces. *Journal of Geophysical Research*, *104*(B1), 817–844. https://doi.org/10.1029/1998jb900007

Ohnaka, M., & Yamashita, T. (1989). A cohesive zone model for dynamic shear faulting based on experimentally inferred constitutive relation and strong motion source parameters. *Journal of Geophysical Research*, *94*(B4), 4089–4104. https://doi.org/10.1029/jb094ib04p04089

Okubo, P. G., & Dieterich, J. H. (1981). Fracture energy of stick-slip events in a large scale biaxial experiment. *Geophysical Research Letters*, *8*(8), 887–890. https://doi.org/10.1029/GL008i008p00887

Okubo, P. G., & Dieterich, J. H. (1984). Effects of physical fault properties on frictional instabilities produced on simulated faults. *Journal of Geophysical Research*, *89*(B7), 5817–5827. https://doi.org/10.1029/JB089iB07p05817

Oohashi, K., Hirose, T., Takahashi, M., & Tanikawa, W. (2015). Dynamic weakening of smectite-bearing faults at intermediate velocities: Implications for subduction zone earthquakes. *Journal of Geophysical Research: Solid Earth*, *120*(3), 1572–1586. https://doi.org/10.1002/2015JB011881

Orellana, L. F., Scuderi, M. M., Collettini, C., & Violay, M. (2018). Do scaly clays control seismicity on faulted shale rocks? *Earth and Planetary Science Letters*, *488*, 59–67. https://doi.org/10.1016/j.epsl.2018.01.027

Paglialunga, F., Passelègue, F. X., Brantut, N., Barras, F., Lebihain, M., & Violay, M. (2021). On the scale dependence in the dynamics of frictional rupture: Constant fracture energy versus size-dependent breakdown work. *Preprint in Earth and Planetary Science Letters*, *584*, 1–33. https://doi.org/10.1016/j.epsl.2022.117442

Paglialunga, F., Passelègue, F. X., Brantut, N., Barras, F., Lebihain, M., & Violay, M. (2022). On the scale dependence in the dynamics of frictional rupture: Constant fracture energy versus size-dependent breakdown work. *Earth and Planetary Science Letters*, *584*, 117442. https://doi.org/10.1016/j.epsl.2022.117442

Palmer, A. C., & Rice, J. R. (1973). The growth of slip surfaces in the progressive failure of over-consolidated clay. *Proceedings of the Royal Society of London*, *332*(1591), 527–548. https://doi.org/10.1098/rspa.1973.0040

Passelègue, F. X., Aubry, J., Nicolas, A., Fondriest, M., Deldicque, D., Schubnel, A., & Di Toro, G. (2019). From fault creep to slow and fast earthquakes in carbonates. *Geology*, *47*(8), 744–748. https://doi.org/10.1130/G45868.1

Passelègue, F. X., Schubnel, A., Nielsen, S., Bhat, H. S., Deldicque, D., & Madariaga, R. (2016). Dynamic rupture processes inferred from laboratory microearthquakes. *Journal of Geophysical Research: Solid Earth*, *121*(6), 4343–4365. https://doi.org/10.1002/2015JB0.12694

Passelègue, F. X., Spagnuolo, E., Violay, M., Nielsen, S., di Toro, G., & Schubnel, A. (2016). Frictional evolution, acoustic emissions activity, and off-fault damage in simulated faults sheared at seismic slip rates. *Journal of Geophysical Research: Solid Earth*, *121*(10), 7490–7513. https://doi.org/10.1002/2016JB012988

Potyondy, D. O., & Cundall, P. A. (2004). A bonded-particle model for rock. *International Journal of Rock Mechanics and Mining Sciences*, *41*(8), 1329–1364. https://doi.org/10.1016/j.ijrmms.2004.09.011

Rabinowicz, E. (1951). The nature of the static and kinetic coefficients of friction. *Journal of Applied Physics*, *22*(11), 1373–1379. https://doi.org/10.1063/1.1699869

Reches, Z., & Lockner, D. A. (2010). Fault weakening and earthquake instability by powder lubrication. *Nature*, *467*(7314), 452–455. https://doi.org/10.1038/nature09348

Rempe, M., Smith, S., Mitchell, T., Hirose, T., & di Toro, G. (2017). The effect of water on strain localization in calcite fault gouge sheared at seismic slip rates. *Journal of Structural Geology*, *97*, 104–117. https://doi.org/10.1016/j.jsg.2017.02.007

Rice, J. R. (2006). Heating and weakening of faults during earthquake slip. *Journal of Geophysical Research*, *111*(5), 1–29. https://doi.org/10.1029/2005JB004006

Rice, J. R., & Cocco, M. (2002). Seismic Fault rheology and earthquake dynamics. *Journal of Geophysical Research*, *107*, 1000–1029.

Riedel, W. (1929). Zur Mechanik geologischer Brucherscheinungen ein Beitrag zum Problem der Fiederspatten. *Zentbl. Miner. Geol. Palaont. Abt.*, 354–368.

Riedmüller, B. G., Brosch, F. J., Klima, K., & Medley, E. W. (2001). Engineering geological characterization of brittle faults and classification of fault rocks. *Engineering Geology*, *19*(April), 13–19.

Rodrigues, R. D. S., da Alves Silva, F. C., & Córdoba, V. C. (2021). Evolution of deformation bands, insights from structural diagenesis. *Journal of Structural Geology*, *143*, 104257. https://doi.org/10.1016/j.jsg.2020.104257

Romanet, P., & Ozawa, S. (2022). Fully dynamic earthquake cycle simulations on a nonplanar fault using the spectral boundary integral element method (sBIEM). *Bulletin of the Seismological Society of America*, *112*(1), 78–97. https://doi.org/10.1785/0120210178

Rummel, F., Alheid, H. J., & Frohn, C. (1978). *Dilatancy and fracture induced velocity changes in rock and their relation to frictional sliding* (Vol. 116). Birkh/iuser Verlag.

Sammis, C. G., & Biegel, R. L. (1989). Fractals, fault-gouge, and friction. *Pure and Applied Geophysics*, *131*(2), 255–271. https://doi.org/10.1007/BF00874490

Sammis, C. G., King, G., & Biegel, R. (1987). The kinematics of gouge deformation. *Pure and Applied Geophysics*, *125*(5), 777–812. https://doi.org/10.1007/BF00878033

Sawai, M., Hirose, T., & Kameda, J. (2014). Frictional properties of incoming pelagic sediments at the Japan trench: Implications for large slip at a shallow plate boundary during the 2011 Tohoku earthquake. *Earth Planets and Space*, *66*(1), 65. https://doi.org/10.1186/1880-5981-66-65

Sawai, M., Shimamoto, T., & Togo, T. (2012). Reduction in BET surface area of Nojima fault gouge with seismic slip and its implication for the fracture energy of earthquakes. *Journal of Structural Geology*, *38*, 117–138. https://doi.org/10.1016/j.jsg.2012.01.002

Schellart, W. P. (2000). Shear test results for cohesion and friction coefficients for different granular materials: Scaling implications for their usage in analogue modelling. *Tectonophysics*, *324*(1–2), 1–16. https://doi.org/10.1016/S0040-1951(00)00111-6

Schmocker, M., Bystricky, M., Kunze, K., Burlini, L., Stünitz, H., & Burg, J.-P. (2003). Granular flow and Riedel band formation in water-rich quartz aggregates experimentally deformed in torsion. *Journal of Geophysical Research*, *108*(B5), 1–16. https://doi.org/10.1029/2002jb001958

Scholz, C. H. (1987). Wear and gouge formation in brittle faulting. *Geology*, *15*(6), 493–495. https://doi.org/10.1130/0091-7613(1987)15<493:WAGFIB>2.0.CO;2

Scholz, C. H. (2002). The mechanics of earthquakes and faulting (2nd ed.). https://doi.org/10.2113/gseegeosci.13.1.81

Scholz, C. H. (2019). *The mechanics of earthquakes and faulting* (3rd ed.). Cambridge University Press. https://doi.org/10.1017/9781316681473

Scholz, C. H., & Engelder, J. T. (1976). The role of asperity indentation and ploughing in rock friction. Part 1: Asperity creep and stick-slip. *International Journal of Rock Mechanics and Mining Sciences & Geomechanics*, *13*(5), 149–154. https://doi.org/10.1016/0148-9062(76)91557-6

Scholz, C. H., Molnar, P., & Johnson, T. (1972). Detailed studies of frictional sliding of granite and implications for the earthquake mechanism. *Journal of Geophysical Research*, *77*(32), 6392–6406. https://doi.org/10.1029/jb077i032p06392

Scuderi, M. M., Carpenter, B. M., & Marone, C. (2014). Physicochemical processes of frictional healing: Effects of water on stick-slip stress drop and friction of granular fault gouge. *Journal of Geophysical Research: Solid Earth*, *119*(5), 4090–4105. https://doi.org/10.1002/2013JB010641

Scuderi, M. M., Collettini, C., Viti, C., Tinti, E., & Marone, C. (2017). Evolution of shear fabric in granular fault gouge from stable sliding to stick slip and implications for fault slip mode. *Geology*, *45*(8), 731–734. https://doi.org/10.1130/G39033.1

Scuderi, M. M., Tinti, E., Cocco, M., & Collettini, C. (2020). The role of shear fabric in controlling breakdown processes during laboratory slow-slip events. *Journal of Geophysical Research: Solid Earth*, *125*(11). https://doi.org/10.1029/2020JB020405

Seyler, C. E., Kirkpatrick, J. D., Savage, H. M., Hirose, T., & Faulkner, D. R. (2020). Rupture to the trench? Frictional properties and fracture energy of incoming sediments at the Cascadia subduction zone. *Earth and Planetary Science Letters*, *546*, 116413. https://doi.org/10.1016/j.epsl.2020.116413

Smith, S. A. F., di Toro, G., Kim, S., Ree, J. H., Nielsen, S., Billi, A., & Spiess, R. (2013). Coseismic recrystallization during shallow earthquake slip. *Geology*, *41*(1), 63–66. https://doi.org/10.1130/G33588.1

Smith, S. A. F., Nielsen, S., & di Toro, G. (2015). Strain localization and the onset of dynamic weakening in calcite fault gouge. *Earth and Planetary Science Letters*, *413*, 25–36. https://doi.org/10.1016/j.epsl.2014.12.043

Spagnuolo, E., Nielsen, S., Violay, M., & Di Toro, G. (2016). An empirically based steady state friction law and implications for fault stability. *Geophysical Research Letters*, *43*(7), 3263–3271. https://doi.org/10.1002/2016GL067881

Tchalenko, J. S. (1970). Similarities between shear zones of different magnitudes. *Geological Society of America Bulletin*, *81*(6), 1625–1640. https://doi.org/10.1130/0016-7606(1970)81[1625:SBSZOD]2.0.CO;2

Togo, T., & Shimamoto, T. (2012). Energy partition for grain crushing in quartz gouge during subseismic to seismic fault motion: An experimental study. *Journal of Structural Geology*, *38*, 139–155. https://doi.org/10.1016/j.jsg.2011.12.014

Togo, T., Shimamoto, T., Ma, S., & Hirose, T. (2011). High-velocity frictional behavior of Longmenshan fault gouge from Hongkou outcrop and its implications for dynamic weakening of fault during the 2008 Wenchuan earthquake. *Earthquake Science*, *24*(3), 267–281. https://doi.org/10.1007/s11589-011-0790-6

Togo, T., Yao, L., Ma, S., & Shimamoto, T. (2016). High-velocity frictional strength of Longmenshan fault gouge and its comparison with an estimate of friction from the temperature anomaly in WFSD-1 drill hole. *Journal of Geophysical Research: Solid Earth*, *121*(7), 5328–5348. https://doi.org/10.1002/2016JB012880

Tullis, T. E. (2015). Mechanisms for friction of rock at earthquake slip rates. *Treatise on Geophysics*, *139*, 139–159. https://doi.org/10.1016/B978-0-444-53802-4.00073-7

Ujiie, K., Tanaka, H., Saito, T., Tsutsumi, A., Mori, J. J., Kameda, J., et al. (2013). Low coseismic shear stress on the tohoku-oki megathrust determined from laboratory experiments. *Science*, *342*(6163), 1211–1214. https://doi.org/10.1126/science.1243485

Vannucchi, P., Spagnuolo, E., Aretusini, S., di Toro, G., Ujiie, K., Tsutsumi, A., & Nielsen, S. (2017). Past seismic slip-to-the-trench recorded in Central America megathrust. *Nature Geoscience*, *10*(12), 935–940. https://doi.org/10.1038/s41561-017-0013-4

Violay, M., Nielsen, S., Gibert, B., Spagnuolo, E., Cavallo, A., Azais, P., et al. (2014). Effect of water on the frictional behavior of cohesive rocks during earthquakes. *Geology*, *42*(1), 27–30. https://doi.org/10.1130/G34916.1

Violay, M., Nielsen, S., Spagnuolo, E., Cinti, D., di Toro, G., & di Stefano, G. (2013). Pore fluid in experimental calcite-bearing faults: Abrupt weakening and geochemical signature of co-seismic processes. *Earth and Planetary Science Letters*, *361*, 74–84. https://doi.org/10.1016/j.epsl.2012.11.021

Walderhaug, O. (1994). Precipitation rates for quartz cement in sandstones determined by fluid-inclusion microthermometry and temperature-history modeling. *Journal of Sedimentary Research: Sedimentary Petrology & Processes*, *64*(2), 324–333. https://doi.org/10.2110/jsr.64.324.(.

Wang, D., Carmeliet, J., Zhou, W., & Dorostkar, O. (2021). On the effect of grain fragmentation on frictional instabilities in faults with granular gouge. *Journal of Geophysical Research: Solid Earth*, *126*(5). https://doi.org/10.1029/2020jb020510

Wawersik, W. R., & Brace, W. F. (1971). Post-failure behavior of a granite and diabase. *Rock Mechanics*, *3*(2), 61–85. https://doi.org/10.1007/bf01239627

Wong, T. (1982). Shear fracture energy of Westerly granite from post-failure behavior. *Journal of Geophysical Research*, *87*(B2), 990–1000. https://doi.org/10.1029/JB087iB02p00990

Woodcock, N. H., & Mort, K. (2008). Classification of fault breccias and related fault rocks. *Geological Magazine*, *145*(3), 435–440. https://doi.org/10.1017/S0016756808004883

Yao, L., Ma, S., Shimamoto, T., & Togo, T. (2013). Structures and high-velocity frictional properties of the Pingxi fault zone in the Longmenshan fault system, Sichuan, China, activated during the 2008 Wenchuan earthquake. *Tectonophysics*, *599*, 135–156. https://doi.org/10.1016/j.tecto.2013.04.011

Zhang, L., & Rummel, F. (1990). Shear fracture energy of rock at high pressure and high temperature. *Physics and Chemistry of the Earth*, *17*(C), 99–109. https://doi.org/10.1016/0079-1946(89)90015-3

Zhao, Z. (2013). Gouge particle evolution in a rock fracture undergoing shear: A microscopic DEM study. *Rock Mechanics and Rock Engineering*, *46*(6), 1461–1479. https://doi.org/10.1007/s00603-013-0373-z

Zhao, Z., Jing, L., & Neretnieks, I. (2012). Particle mechanics model for the effects of shear on solute retardation coefficient in rock fractures. *International Journal of Rock Mechanics and Mining Sciences*, *52*, 92–102. https://doi.org/10.1016/j.ijrmms.2012.03.001